1.156-GHz Self-Aligned Vibrating Micromechanical Disk Resonator

Jing Wang, *Student Member, IEEE*, Zeying Ren, and Clark T.-C. Nguyen, *Senior Member, IEEE*

***Abstract*—A new fabrication methodology that allows self-alignment of a micromechanical structure to its anchor(s) has been used to achieve vibrating radial-contour mode polysilicon micromechanical disk resonators with resonance frequencies up to 1.156 GHz and measured *Q*'s at this frequency >2,650 in both vacuum and air. In addition, a 734.6-MHz version has been demonstrated with *Q*'s of 7,890 and 5,160 in vacuum and air, respectively. For these resonators, self-alignment of the stem to exactly the center of the disk it supports allows balancing of the resonator far superior to that achieved by previous versions (in which separate masks were used to define the disk and stem), allowing the present devices to retain high *Q* while achieving frequencies in the gigahertz range for the first time. In addition to providing details on the fabrication process, testing techniques, and experimental results, this paper formulates an equivalent electrical circuit model that accurately predicts the performance of these disk resonators.**

I. Introduction

VIBRATING mechanical tank components, such as quartz crystals and surface acoustic wave (SAW) resonators with Q's in the range of 10^3–10^6, are widely used to implement high-Q oscillators and bandpass filters in the radio frequency (RF) and intermediate frequency (IF) stages of communication transceivers. Due to orders of magnitude higher quality factor Q, filters using such technologies greatly outperform comparable filters implemented using conventional transistor technologies in insertion loss, percent bandwidth, achievable rejection, and dynamic range [1]–[5]. Oscillators also benefit substantially from high Q, as their phase noise at important offesets is often inversely proportional to the square of Q [6]. Unfortunately, however, the crystal and SAW devices that provide beneficial high Q's are off-chip components that must interface with transistor electronics at the board level, posing a significant bottleneck against the ultimate miniaturization of wireless communicators, and trumpeting a need for on-chip replacements.

Note that, although low-capacitance integration with transistor electronics would be beneficial, the phrase "on-chip" does not necessarily imply integration with transistors. In fact, an "on-chip" resonator technology that does not include transistors, but that integrates numerous micromechanical circuits (e.g., filters) onto a single chip, would already be quite beneficial to wireless architectures targeting impending needs for multiband reconfigurability in future handsets. Such architectures will likely require high-Q front-end RF filters in large quantities—perhaps one set for each wireless standard to be addressed. Fig. 1 compares the simplified system block diagram for a present-day handset receiver (assuming a super-heterodyne architecture) with one targeted for multiband applications, clearly showing that a larger number of switchable high-Q RF filters with frequencies in the 800 MHz to 2.4 GHz range, Q's in the >500 range, and temperature coefficients commensurate with present RF preselect and image-reject filter requirements (e.g., ~40 ppm/°C), will soon be required for wireless applications. Given the rather large size and cost required to implement the RF preselect filter bank of Fig. 1(b) using discrete resonators and filters, a technology capable of realizing numerous such filters (and the resonators that compose them) onto a single chip in a single planar fabrication process would be most welcome. If such on-chip resonators also exhibited Q's >10,000, then RF channel-selection (as opposed to band-selection) might even be possible, as would gigahertz reference oscillators with exceptionally low power consumption [7], [8]. For an oscillator application, however, the temperature stability of the resonator also would need to be commensurate with that of present-day low frequency reference oscillators, on the order of 2 ppm total frequency excursion (at 13 MHz) over at least the 0–70°C commercial temperature range, and for some cases over the −40°C to +85°C industrial temperature range.

With Q's often exceeding 10,000, vibrating micromechanical (μmechanical) resonators are emerging as viable candidates for on-chip versions of the high-Q resonators used in wireless communication systems [8] for both frequency generation and filtering. To date, nano-scale versions in silicon carbide have now reached 1 GHz in frequency at cryogenic temperatures near 4 K [9], but their Q's have not exceeded 500; and these nano-scale devices so far are too small to handle the power magnitudes used in present-day communications. Nano-scale resonators are also more susceptible to scaling-induced performance limitations, such as the adsorption/desorption noise and temperature fluctuation noise postulated in [10], than micro-scale counterparts. Although micro-scale versions in polysilicon with greater power handling ability and considerably less susceptibility to scaling-induced noise mechanisms have reached published frequencies up to the

Manuscript received November 19, 2003; accepted July 8, 2004. This work was supported by DARPA and an NSF ERC in Wireless Integrated Microsystems.

The authors are with the Department of Electrical Engineering and Computer Science, University of Michigan, Ann Arbor, MI 48109-2122 (e-mail: jingw@umich.edu, ctnguyen@umich.edu).

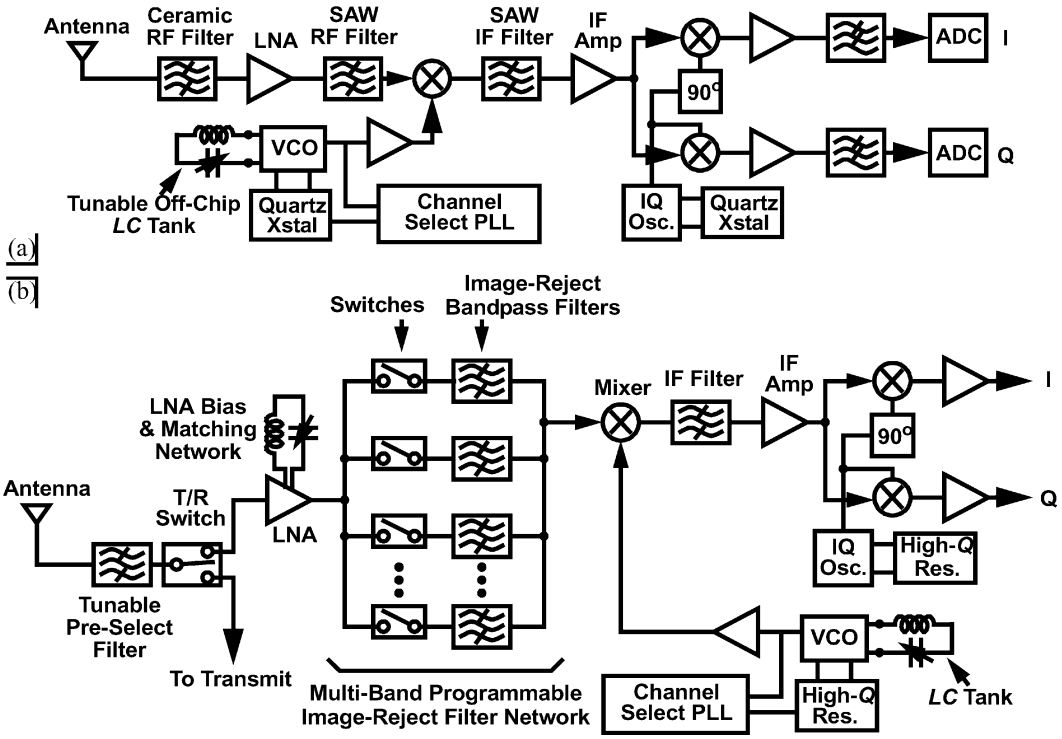

Fig. 1. Expected progression of transceiver front-end architectures as multiuse wireless applications become more prevalent. (a) Present-day superheterodyne. (b) Next generation multiband architecture in which the number of RF filters needed could reach greater than 15. As explained in the text, the switches in (b) are unnecessary and can be removed if the capacitively driven resonators of this work are used in the filters, since these resonators are on/off switchable via their bias voltages.

mid-VHF range (156 MHz [11], [12]) with Q's exceeding 10,000; have been demonstrated with temperature coefficients as small as -0.24 ppm/°C [13]; and have been used as reference tanks in oscillators that practically satisfy the -130 dBc/Hz at 1 kHz offset from a 13 MHz carrier Global System for Mobile Communications (GSM) reference oscillator phase noise specification [14]. However, the acceptance of such devices for RF filtering applications in present-day communication transceivers has been hindered so far by several remaining issues, including: (1) a frequency range that had not surpassed 1 GHz, (2) the need for vacuum to attain high Q, and (3) higher impedances than normally exhibited by macroscopic high-Q resonators.

This work now alleviates the first two of the above issues. In particular, polysilicon micromechanical radial-contour mode vibrating disk resonators featuring new self-aligned stems have been demonstrated with record resonance frequencies up to 1.156 GHz and measured Q's at this frequency >2,650 in both vacuum and air, and at room temperature. In addition, a 734.6-MHz version has been demonstrated with Q's of 7,890 and 5,160 in vacuum and air, respectively [15]. For these resonators, self-alignment of the stem to exactly the center of the disk it supports allows symmetrical balancing of the resonator far superior to that achieved by previous versions (where separate masks were used to define the disk and stem [11]), allowing the present devices to retain high Q while achieving frequencies in the gigahertz range for the first time, and all while retaining the micro-scale dimensions and high stiffnesses required for adequate power handling. In addition, the use of more rugged polysilicon electrodes (as opposed to the malleable metal used in previous disks [11]) greatly improves the yield of these devices; and the introduction of a substrate ground plane that steers away feedthrough current greatly facilitates the measurement of their ultra high frequency characteristics.

This paper details the design, modeling, fabrication, and testing of stem-self-aligned, contour-mode disk resonators operating in fundamental and higher modes. After a qualitative description of device structure and operation in Section II, an equivalent circuit model is developed in Section III to allow accurate prediction of its electrical performance. Following brief discussions in Sections IV and V on the expected Q in air and the impact of stem misalignment, respectively, Section VI then proceeds with a step-by-step description of the fabrication methodology used to achieve self-aligned micromechanical disks, the test results of which are detailed and compared against theory in Section VII. The paper concludes (Section VIII) with a brief exposition on the limitations of this prototype design, followed by suggestions for overcoming them in future renditions.

II. Resonator Structure and Operation

Fig. 2 presents the perspective-view schematic of a self-aligned disk resonator identifying key features, defining

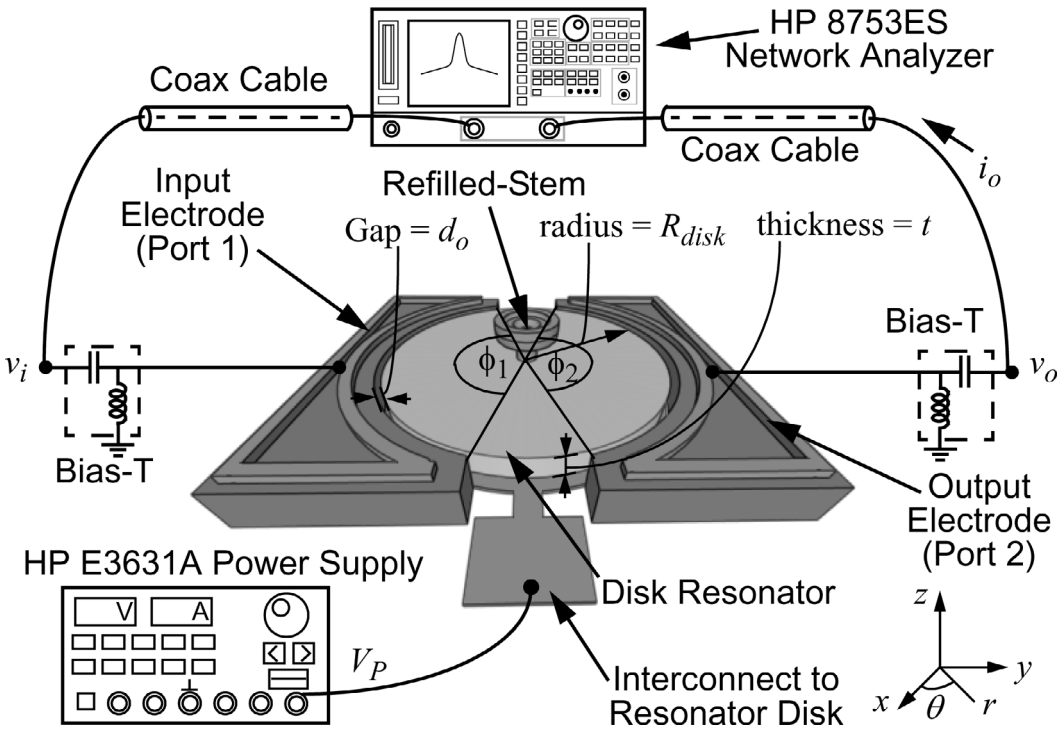

Fig. 2. Perspective-view schematic of a self-aligned disk resonator identifying key features and showing a two-port measurement scheme.

axes and directions to be used in model derivations, and illustrating a two-port bias, excitation, and measurement scheme. As shown, this device consists of a polysilicon disk suspended by a stem, self-aligned to its center, and enclosed by two polysilicon capacitive transducer electrodes spaced less than 100 nm from the disk perimeter. Aside from variants to be specified later, the typical disk thickness used in this work is 2 μm, and most stems have diameters of 2 μm and heights of 0.7 μm from the substrate to the disk bottom. In the schematic, the tops of the electrodes have been rendered transparent to enable viewing of the underlying structure.

A. Resonator Operation

The resonators of this work use capacitive transduction in large part to simplify future integration with transistor circuits. To excite the device of Fig. 2 in its two-port configuration, a direct current (DC)-bias voltage V_P is applied to the disk and an alternating current (AC) signal v_i to its input electrode. Note that the application of the DC-bias V_P serves only to charge the electrode-to-disk capacitance, and thereby, does not incur power consumption. Together, these voltages generate an electrostatic input force F_i in a radial direction (pointing outward from the disk) given by [16]:

$$F_i = \frac{1}{2}\left(\frac{\partial C_1}{\partial r}\right)(V_P - v_i)^2 \cong -V_P\left(\frac{\partial C_1}{\partial r}\right)v_i, \quad (1)$$

where only the dominant term at resonance has been retained (i.e., components at DC and at frequencies different from v_i have been neglected), and where $\partial C_1/\partial r$ is the change in electrode-to-resonator overlap capacitance per unit radial displacement at the input port (i.e., port 1). An expression for $\partial C_1/\partial r$ can be obtained from the expression for the port 1 electrode-to-resonator overlap capacitance $C_1(r)$ as follows:

$$C_1(r) = C_o\left(1 - \frac{r}{d_o}\right)^{-1} \quad \Rightarrow \quad \frac{\partial C_1}{\partial r} = \frac{C_o}{d_o}\left(1 - \frac{r}{d_o}\right)^{-2}, \quad (2)$$

where C_o is the static drive electrode-to-disk capacitance. If displacements are small, (2) can be expanded to obtain the more useful form (for later) [17]:

$$\frac{\partial C_1}{\partial r} = \left(\frac{C_o}{d_o}\right)\left(1 + A_1 r + A_2 r^2 + A_3 r^3 + \cdots\right), \quad (3)$$

where

$$A_1 = \frac{2}{d_o},\ A_2 = \frac{3}{d_o^2},\ A_3 = \frac{4}{d_o^3}. \quad (4)$$

For the present purpose of obtaining a linear model for the disk resonator, $\partial C_1/\partial r$ can be approximated by the first term in (3), which then can be expanded into:

$$\frac{\partial C_1}{\partial r} \approx \frac{\varepsilon_o \phi_1 R_{disk} t}{d_o^2}, \quad (5)$$

where R_{disk} and t are the radius and thickness, respectively, of the disk; ε_o is the permittivity in vacuum; d_o is the electrode-to-resonator gap spacing; and ϕ_1 is the angle defined by the edges of the input electrode (i.e., electrode 1), as indicated in Fig. 2. When the frequency of v_i matches the radial-contour mode resonance frequency of

the disk, the resulting force drives the disk into a vibration mode shape in which it expands and contracts radially around its perimeter, in a fashion reminiscent of breathing, with a zero-to-peak radial displacement amplitude at any point of the disk (r, θ) given by [18]:

$$\Re(r, \theta) = AhJ_1(hr), \tag{6}$$

and at the perimeter (i.e., $r = R_{disk}$) in phasor form by:

$$\Re\left(R_{disk}, \theta\right) = \frac{QF_i}{jk_{re}}, \tag{7}$$

where k_{re} is the effective stiffness at a location on the perimeter (to be analytically specified later in Section III); R_{disk} is the disk radius; $\omega_o = 2\pi f_o$ is the angular resonance frequency; $J_n(y)$ is the Bessel function of the first kind of order n; ρ, σ, and E are the density, Poisson ratio, and Young's modulus, respectively, of the structural material; A is a drive force-dependent ratio [18], specified later in Section VII's design tables; and h is a constant defined as:

$$h = \sqrt{\frac{\omega_o^2 \rho}{\left(\frac{2E}{2+2\sigma} + \frac{E\sigma}{1-\sigma^2}\right)}}. \tag{8}$$

The radial vibration of the disk creates a DC-biased (by V_P) time-varying capacitance between the disk and output electrode that then sources an output motional current i_o proportional to the amplitude of vibration (radial displacement) given by:

$$\begin{aligned} i_o &= V_P \left(\frac{\partial C_2}{\partial r}\right) \frac{\partial \Re\left(R_{disk}, \theta\right)}{\partial t} \\ &= \omega_o \frac{Q}{k_{re}} \left(\frac{\partial C_1}{\partial r}\right) \left(\frac{\partial C_2}{\partial r}\right) V_P^2 v_i, \end{aligned} \tag{9}$$

where (1) and (7) have been used, and where $\partial C_2/\partial x$ is the change in electrode-to-resonator overlap capacitance per unit radial displacement at the output port (i.e., port 2), which takes on a form similar to that of (5), but with ϕ_1 replaced by ϕ_2. In effect, this device operates by first converting the input electrical signal v_i to a mechanical force F_i, which is filtered by the high-Q mechanical response of the resonator, allowing only components at the disk resonance frequency to be converted to a disk displacement $\Re(r, \theta)$ [or velocity $v(r, \theta)$]. This mechanical domain displacement then is converted back to the electrical domain into the output current i_o by action of the output electrode capacitive transducer. It should be noted that output current is only generated if the DC-bias voltage V_P is finite. If the DC voltage between the output electrode and disk is set to zero, then no current flows, and the device is effectively "off." Thus, V_P provides an on/off switchability for this device.

With the AC input voltage applied to an electrode that overlaps only half the disk, the two-port excitation scheme of Fig. 2 actually generates a nonsymmetric force applied to the input side of the disk. As long as the AC input is at the radial contour-mode resonance frequency—whether the force is symmetric or not—the symmetric radial contour-mode shape will ensue, with negligible distortion according to ANSYS (ANSYS, Inc., Canonsburg, PA) finite-element simulation. One issue, however, with an asymmetric forcing geometry is that other vibration modes can be excited if the input frequency matches their respective resonance frequencies—something that would be much less of an issue if the forcing geometry were completely symmetric, such as would be the case if the input electrode completely surrounded the resonator, and the output were taken out of the resonator-bias electrode, with the device operated as a one port [19]. According to ANSYS finite-element simulation, there are several vertical modes within a 30% range of the center frequency of a given disk, but these are neither excitable nor detectable by the lateral electrode configuration used. In addition, of the few lateral modes, only the wine-glass mode [20] depicted in Fig. 3, at about two-thirds the radial mode frequency, is amenable to excitation via the lateral two-port electrode configuration of Fig. 2. At two-thirds the radial-mode frequency, this mode is not likely to be troublesome in most applications.

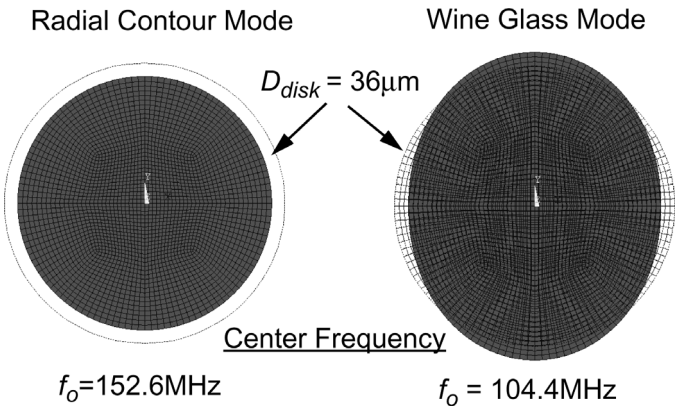

Fig. 3. Comparison of the 152-MHz radial contour mode and the 104-MHz wine-glass mode (closest spurious mode) for a 36-μm diameter polysilicon disk resonator simulated via ANSYS 6.0, demonstrating frequency separation of about 50 MHz between the two.

In actual measurement, the only detectable spurious mode was indeed the wine-glass mode, and this mode was only intermittently measurable on disks operated in two-port mode with (purposely) misaligned stems. Disks with self-aligned (i.e., perfectly centered) stems did not exhibit any measurable spurious modes in the vicinity of the fundamental radial-contour mode frequency.

B. Resonance Frequency Design

The dimensions needed to attain a specified nominal resonance frequency f_{onom} for a radial-contour mode disk can be obtained by solving the mode frequency equation, given by [18]:

$$\delta \times \frac{J_0(\delta)}{J_1(\delta)} = 1 - \sigma, \tag{10}$$

where

$$\delta = \omega_{onom} R_{disk} \sqrt{\frac{\rho\left(1-\sigma^2\right)}{E}}, \tag{11}$$

and where ω_{onom} is the nominal radian resonance frequency for a purely mechanical system (i.e., with no applied electrical signals, hence no electrical stiffness [16]). By sacrificing some degree of accuracy, (10) and (11) can be rendered into the more intuitive form [21];

$$f_{onom} = \frac{\alpha\kappa}{R_{disk}} \sqrt{\frac{E}{\rho}}, \tag{12}$$

where κ is a parameter dependent upon Poisson's ratio ($\kappa = 0.342$ MHz/μm for polysilicon), and α is a mode-dependent scaling factor that accounts for higher order modes. (Values for specific designs are included in Table I of Section VII.)

As seen in (10), (11), or (12), the frequency of resonance is a strong function of structural material properties and of geometry, in particular, of the disk radius—a lateral dimension. The strong dependence of the resonance frequency on a lateral dimension means that attaining a desired resonance frequency is merely a matter of proper computer-aided design (CAD) layout. Thus, a single fabrication process run (such as described in Section VI) with a single structural layer deposition step can yield resonators covering a very diverse frequency range, all specified by CAD layout. This constitutes a major advantage of this capacitively-transduced resonator over the class of piezoelectric resonators whose resonance frequencies are governed mainly by film thickness, such as quartz crystals or thin-film bulk acoustic resonators (FBAR's). For these types of resonators, a new fabrication run, or at least multiple film depositions, are required to achieve the several different frequencies needed for future multiband reconfigurable wireless applications. The ability of the present disk resonator design to achieve many different frequencies in one process run, together with its potential for low-capacitance integration with transistor electronics and a convenient on/off switchability function [22] that dispenses with any need for low-loss switches, makes the described disk resonator an attractive choice for the switchable filter bank chip described in Section I. (If the filters in the bank of Fig. 1(b) use the radial-mode disk resonators of this work, the switches can be removed!)

C. Frequency Pulling Via Electrical Stiffness

Because the electrode-to-resonator capacitance is a nonlinear function of the disk radial displacement, there are actually many more force components generated than represented in (1). In particular, expanding (1) further and inserting the first two terms of (3) yields:

$$\begin{aligned} F_i &= \frac{1}{2}\frac{C_o}{d_o}\left(V_P^2 - 2V_P v_i + v_i^2 + A_1 V_P^2 r - 2A_1 V_P v_i r + A_1 v_i^2 r\right) \\ &= \frac{1}{2}\frac{C_o}{d_o}\left(\ldots - 2V_P v_i + A_1 V_P^2 r + A_1 v_i^2 r + \ldots\right), \end{aligned} \tag{13}$$

where the last form includes only terms that can generate components at resonance. Expanding the last form of (13), inserting the first equation in (4), and inserting $v_i = V_i \cos\omega_o t$ and $r = \Re \sin\omega_o t$ (where the fact that the displacement r is 90° phase-shifted from v_i has been accounted for) yields:

$$\begin{aligned} F_i = \\ -\left[V_P \frac{C_o}{d_o} V_i \cos\omega_o t - \left(V_P^2 + \frac{V_i^2}{2}\right)\left(\frac{C_o}{d_o^2}\right)\Re \sin\omega_o t\right], \end{aligned} \tag{14}$$

where the second term is at the resonance frequency, but in quadrature with the input force (i.e., the first term) and proportional to the displacement amplitude $\Re$—both qualities also exhibited by the mechanical spring restoring force of the resonator. However, although the mechanical spring restoring force generally acts to oppose an input force, this force acts to increase the input force. In effect, the second term in (14) can be interpreted as an electrical spring constant of the form:

$$k_{en} = \left(V_P^2 + \frac{V_i^2}{2}\right)\frac{\varepsilon_o \phi_n R_{disk} t}{d_o^3},\ n = 1, 2, \tag{15}$$

which has been generalized using n to reflect the fact that all electrodes will contribute an electrical stiffness. The electrical stiffnesses of all electrodes, regardless of their position [17], subtract from the mechanical spring constant of the beam k_m, changing its resonance frequency to:

$$\begin{aligned} f_o &= \sqrt{\frac{k_{re}}{m_{re}}} = \sqrt{\frac{k_m - k_{e1} - k_{e2}}{m_{re}}} \\ &= f_{nom}\left[1 - \frac{(k_{e1} + k_{e2})}{k_m}\right]^{1/2} \\ &\cong f_{nom}\left[1 - \frac{1}{2}\frac{(k_{e1} + k_{e2})}{k_m}\right], \end{aligned} \tag{16}$$

where m_{re} is the effective stiffness of the disk at any point on its perimeter; k_{re} is the effective stiffness at that same location with all voltages applied; k_m is the purely mechanical stiffness (i.e., with no voltages applied) of the disk at that same location; and the last expression used the binomial expansion to approximate f_o for the case in which the mechanical stiffness is many times larger than any of the electrical stiffnesses, which is generally the case for the devices of this work. Rearrangement of (16) yields for the fractional frequency change due to electrical-stiffness-related parameters, for the very common case where $V_P \gg V_i$ [26]:

$$\frac{\Delta f}{f_o} = -\frac{1}{2}\frac{(k_{e1} + k_{e2})}{k_m} = -\frac{1}{2}\frac{V_P^2}{k_m} \cdot \frac{\varepsilon_o R_{disk} t}{d_o^3} \cdot (\phi_1 + \phi_2). \tag{17}$$

For high frequency (HF) and very high frequency (VHF) resonators, the value of k_m ranges from 500 N/m to 100,000 N/m, respectively, which are generally much larger than that of their k_e's but still of a size that allows fractional frequency shifts ranging from 0.1–10% (from VHF

to HF) [12], [16]. As will be seen in the next and succeeding sections, the UHF disk resonators of this work have k_m's on the order of 1–100 MN/m, which are so high compared with their k_e's (which are still on the same order as for HF and VHF resonators), that fractional frequency shifts on the order of only 1–100 ppm ensue. In particular, for the 20-μm diameter, 2.1-μm thick 1.156 GHz radial-contour mode disk of this work with $V_P = 10.5$ V and $d_o = 68$ nm, $k_m = 75.5$ MN/m and $(k_{e1} + k_{e2}) = 529.5$ N/m, for which (17) yields 3.5 ppm, which is much smaller than variations expected from just temperature dependence. Note, however, that with smaller gaps on the order of 10 nm, appreciable frequency shifts of up to 5 MHz can still be obtained in the same resonator over a V_P range of 20 V. Thus, the degree of tunability is still a strong function of design.

For the case where the high stiffness of disk resonators precludes tunability by the DC-bias V_P often used by HF and VHF resonators, it also suppresses mechanisms for instability (e.g., temperature dependence of the electrode-to-resonator gap spacing d_o [23], microphonics, etc.), perhaps making for an overall zero sum gain from a design perspective.

D. Temperature Dependence of the Resonance Frequency

Historically, the temperature stability of HF and VHF micromechanical resonators have been governed by a combination of the temperature dependencies of: the electrical stiffness (i.e., the electrode-to-resonator gap d_o); the Young's modulus E; and resonator dimensions. Of the three, the electrical stiffness temperature dependence is the most amenable to design, and actually can be designed to dominate over the others with the right choice of DC-bias V_P and electrode-to-resonator gap spacing d_o. This fact that had recently been used to strategically null out the temperature coefficient of a clamped-clamped beam micromechanical resonator down to only -0.24 ppm/°C by designing in an electrode-to-resonator gap spacing that varied with temperature so as to cancel out frequency shifts due to Young's modulus temperature dependence [13].

But, as mentioned above, the much larger mechanical stiffnesses of the disk resonators of this work greatly reduce the influence of electrical stiffness (i.e., of electrode-to-resonator gap spacing) on the resonance frequency, perhaps to the point at which it simply can be neglected compared to the other temperature dependences in many cases. To verify that this is the case, the fractional frequency change with temperature due to a change in electrode-to-resonator gap spacing d can be obtained by taking the partial derivative of (17) with respect to temperature to yield:

$$\frac{\partial\left(\Delta f/f_o\right)}{\partial T} = \frac{\partial\left(\Delta f/f_o\right)}{\partial d}\frac{\partial d}{\partial T} = \frac{3}{2}\frac{\left(V_P^2 + 0.5V_i^2\right)}{k_m}\frac{\varepsilon_o\left(\phi_1+\phi_2\right)R_{disk}t}{d_o^4}\left[\alpha_{Si}d_o + \left(\alpha_{Si}-\alpha_e\right)L_e\right], \quad (18)$$

where α_{Si} and α_e are the thermal expansion coefficients of silicon and of the surrounding electrode, respectively; and L_e is the suspended electrode length, indicated in Fig. 6(b).

For the case of a polysilicon electrode (i.e., this work), $\alpha_{Si} = \alpha_e = 2.6$ ppm/°C, so $\partial d/\partial T = \alpha_{Si}d_o$. For the largest resonator of this work (i.e., worst case), for which $R_{disk} = 36$ μm, $t = 2.1$ μm, $L_e = 5$ μm, $d_o = 87$ nm, $k_m = 3.52$ MN/m, $V_P = 6$ V, and $V_i = 0.25$ V, (18) yields 1.2×10^{-4} ppm/°C, which is extremely small—on the order of resonance frequency temperature coefficients typically exhibited by oven-controlled crystals [24]. Even if gold metal electrodes were used, such as in [11] or [23], for which $\alpha_e = 13$ ppm/°C, (18) still yields only -0.027 ppm/°C, which is equally negligible compared with typical resonator temperature coefficients. This is not to say, however, that a large temperature dependence on the gap spacing cannot be achieved. If the gap were reduced to 15 nm, (18) yields -30.5 ppm/°C, which is enough to compensate using the technique of [13] (with the right geometric design changes).

For gap spacing greater than 20 nm, the temperature coefficient of the resonance frequency for a disk resonator is governed mainly by the temperature dependencies of the Young's modulus of its structural material and its own dimensions. Differentiating (12) with respect to temperature and dividing by f_o yields the following expression for the fractional resonance frequency change versus temperature (i.e., the temperature coefficient):

$$TC_f = \frac{1}{f_o}\frac{\partial f}{\partial T} = \left(-\frac{1}{R_{disk}}\frac{\partial R_{disk}}{\partial T} + \frac{1}{2}\frac{1}{E}\frac{\partial E}{\partial T}\right) = -\alpha_{poly} + \frac{1}{2}TC_E, \quad (19)$$

where α_{poly} is the thermal expansion coefficient of polysilicon (-2.6 ppm/°C) and TC_E is the temperature coefficient of its Young's modulus (-40 ppm/°C [25]). Plugging in numbers, (19) yields a predicted polysilicon disk resonator temperature coefficient of about -22.6 ppm/°C. Section VII will present actual temperature coefficient measurements.

III. Electrical Equivalent Circuit

To conveniently model and simulate the impedance behavior of this mechanical resonator when used in an electromechanical circuit, an electrical equivalent circuit is needed. Despite its mechanical nature, the disk resonator of Fig. 2 still looks like an electrical device when looking into its ports, and so can be modeled by either of the electrical inductor-capacitor-resistor (LCR) equivalent circuits shown in Fig. 4. The values for the elements in these LCR equivalents are governed by the total integrated kinetic energy in the resonator, by its mode shape, and by parameters associated with its transducer ports [16], [21].

The total kinetic energy in a vibrating disk can be obtained by integrating the kinetic energies of all infinitesimal mass elements dm in the disk, and can be expressed as:

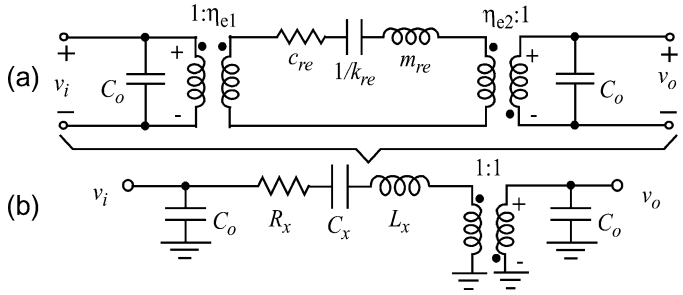

Fig. 4. Equivalent circuit models for a two-port disk resonator. (a) Physically consistent model using actual values of mass and stiffness for elements. (b) Purely electrical model.

$$KE_{tot} = \frac{1}{2}\int_0^{2\pi}\int_0^{R_{disk}} dm \times v^2(r,\theta), \tag{20}$$

where $v(r,\theta)$ is the velocity magnitude at location (r,θ) given by:

$$v(r,\theta) = \omega\Re(r,\theta) = \omega A h J_1(hr), \tag{21}$$

where ω is the radian frequency of motion and where:

$$dm = \rho \times t \times r d\theta \times dr, \tag{22}$$

is a mass element. Inserting (21) and (22) into (20), the total kinetic energy of a vibrating disk resonator reduces to:

$$KE_{tot} = A^2\omega^2 h^2 \pi\rho t \int_0^{R_{disk}} r J_1^2(hr) dr. \tag{23}$$

The equivalent mass at a location (r,θ) can be obtained by dividing the total kinetic energy by one-half the square of the velocity at that location [21]. Doing so for the case of a location (R_{disk},θ) on the perimeter of the disk yields:

$$m_{re} = \frac{KE_{tot}}{\frac{1}{2}v^2\left(R_{disk},\theta\right)} = \frac{2\pi\rho t\int_0^{R_{disk}} r J_1^2(hr)dr}{J_1^2\left(hR_{disk}\right)}. \tag{24}$$

From (24), expressions for the equivalent stiffness and damping at a location on the disk perimeter can be obtained using the relations:

$$k_{re} = \omega_o^2 m_{re}, \tag{25}$$

$$c_{re} = \frac{\omega_o m_{re}}{Q} = \frac{\sqrt{k_{re}m_{re}}}{Q}. \tag{26}$$

where ω_o is the radian resonance frequency that includes the effect of electrical stiffness. Eq. (24)–(26), together with the expression for the electromechanical coupling factor at port n:

$$\eta_{en} = V_P\left(\frac{\partial C_n}{\partial x}\right), \text{ where } n = 1,2, \tag{27}$$

round out all element values needed in the physically consistent equivalent circuit of Fig. 4(a), which is the more general of the two in this figure because it supports more general I/O port configurations. However, for direct comparison with the equivalent circuits of other tank circuits, and for a greater ease in intuitive circuit analysis, the purely electrical equivalent circuit of Fig. 4(b) is oftentimes preferred. The element values for this circuit are obtained from the mechanical lumped element values of (24)–(26) by reflecting them through the transformers via the expressions:

$$L_x = \frac{m_{re}}{\eta_{e1}\eta_{e2}} \quad C_x = \frac{\eta_{e1}\eta_{e2}}{k_{re}} \quad R_x = \frac{c_{re}}{\eta_{e1}\eta_{e2}}. \tag{28}$$

The C_o in each circuit of Fig. 4 represents capacitance from an I/O electrode to AC ground, and as such, is primarily composed of a combination of electrode-to-resonator overlap capacitance and electrode-to-substrate capacitance.

Of the elements in (28), the series motional resistance R_x is often the one that most influences practical applications, which generally prefer smaller values of R_x in order to match correctly to the typical 50 Ω to 377 Ω impedances of existing systems. Using (5), (26), and (27) in the last expression of (28), the expression for R_x can be condensed to:

$$R_x \approx \frac{\omega_o m_{re}}{Q}\cdot\frac{1}{V_P^2}\cdot\frac{d_o^4}{\phi_1\phi_2\left(\varepsilon_o R_{disk} t\right)^2}. \tag{29}$$

Eq. (29) implies that R_x can be reduced by increasing the DC-bias voltage V_P, increasing the disk thickness t, or decreasing the electrode-to-disk gap spacing d_o (on which R_x depends quite strongly, to the fourth power). The DC-bias voltage V_P can sometimes be constrained by the system power supply voltage, or by the pull-in voltage of the resonator [26], at which electrostatic forces overcome the static stiffness of the resonator structure and pull it into its electrodes, often resulting in catastrophic destruction of the device if its surface is not coated by a dielectric of sufficient thickness. The electrode-to-disk gap and disk thickness are constrained by the limitations of the fabrication process, which as will be seen in Section VI, does allow for quite aggressive scaling of the gap.

It also should be noted that, when $V_P = 0$ V, the series motional resistance R_x is infinite, so the resonator (or filter constructed of several resonators) is effectively off. This convenient on/off switchability via mere application or removal of the DC-bias voltage V_P represents yet another advantage of capacitive transduction over piezoelectric. In particular, whereas a filter composed of piezoelectric resonators would require (lossy) switches in series to switch it in and out of a filter bank, a filter composed of the capacitively transduced disks of this work would not require series switches. Rather, the DC-bias voltage V_P can be used to switch a given filter in and out (i.e., the filter is off when $V_P = 0$ V, and on when V_P is a finite voltage) and all realized via electronics outside of the signal path. As mentioned previously, it is this feature that allows the switchable filter bank of Fig. 1(b) to be implemented without the need for the low-loss series switches shown.

IV. Vacuum-Less Device Operation

The need for vacuum to attain high Q by previous micromechanical resonators with frequencies at HF or below is very well documented [16], [26]–[28]. In fact, it is this requirement for vacuum that has historically deflected potential users away from microelectromechanical systems (MEMS) resonator technology. Clearly, a micromechanical resonator design that did not need vacuum to attain high Q could very quickly change user perceptions. The radial-contour mode micromechanical disk of this work is one such resonator.

In particular, one important difference between the stiff, high-frequency resonators of this work and previous lower frequency ones is the difference in total energy per cycle. In particular, the peak kinetic energy per cycle for a given mechanical resonator can be computed via the generalized expression:

$$KE_{peak} = \frac{1}{2} m_{re} (\omega_o X)^2 = \frac{1}{2} k_{re} X^2, \tag{30}$$

where X and k_{re} are the peak displacement and effective stiffness, respectively, at a given location. Given that the $k_{re} \sim 75.5$ MN/m for a point on the perimeter of a 1.156-GHz, 20-μm diameter, 2.1-μm thick disk resonator is more than 50,000 times the 1,500 N/m typical at the midpoint of a 10 MHz clamped-clamped beam (CC-beam); the former is expected to store 50,000 times more energy per cycle for the same displacement amplitude. With energies per cycle many times larger than those of previous, more-compliant devices, the resonators of this work—and virtually any high stiffness, high-frequency, micromechanical resonator device—are expected to lose a much smaller percentage of their total energy to viscous gas damping. In addition, at frequencies this high, the surrounding air begins to behave more like a spring than a damper, thereby reducing energy losses due to gas damping from the start. As a result of both of these effects, high-frequency micromechanical resonators (disks or other types) are expected to exhibit high Q even under air-damped conditions.

That air damping is much less of a problem for high frequency disk resonators also has been predicted by finite-element simulation [29]. Section VII will present actual measurements as ultimate verification.

V. Stem Size and Placement

As previously mentioned, the key feature of this work that allows radial contour-mode disk resonators to achieve frequencies above 1 GHz while retaining exceptional Q is self-alignment (i.e., exact placement) of the stem at the very center of the disk. In particular, because the motion of a disk in its radial-contour mode is symmetric and purely radial for fundamental and higher modes, its center corresponds to a motionless nodal point during vibration. Self-alignment of the stem to exactly the center of the disk it supports, as shown in Fig. 2, then minimizes energy loss to the substrate through the stem anchor, allowing high-Q operation despite the high stiffness characteristic of disk designs.

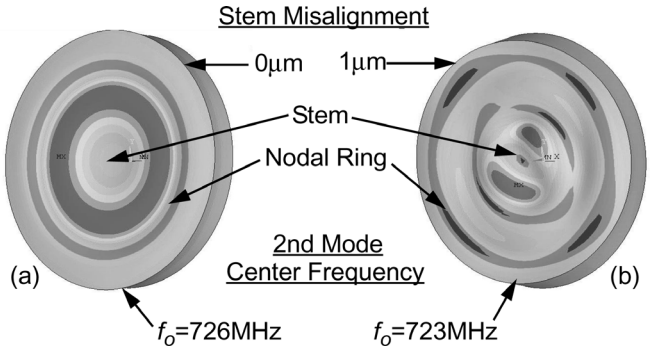

Fig. 5. ANSYS 6.0 modal displacement simulation for a 20-μm diameter, 2-μm stem, radial-contour mode disk with roughly 10,000 radially meshed planar elements for the cases of (a) a perfectly centered stem, and (b) a stem offset from the center by only 1 μm.

To illustrate the importance of perfect alignment, Fig. 5 presents finite element modal analyses on a 20-μm diameter radial-contour mode disk with a 2-μm diameter stem using ANSYS 6.0 with radially meshed planar elements no larger than 0.5 μm for the cases of: (a) a perfectly centered stem, and (b) a stem offset from the center by only 1 μm. Here, a perfectly centered stem leads to a symmetric and purely radial second contour mode shape shown in Fig. 5(a). Conversely, even just 1 μm of misalignment leads to dramatic mode shape distortions depicted by Fig. 5(b) and consequent acoustic energy losses to the substrate that lower the Q, making resonance detection difficult. This reduction in Q due to stem misalignment is verified in Section VII, which presents actual measurements on disk resonators whose stems have been purposely located off-center, showing substantial reductions in device Q.

In addition to lower Q, the measured devices of Section VII with stems purposely misaligned by 0.5 μm exhibited 3–4X lower pull-in voltages [26] than perfectly aligned versions, perhaps a result of the force imbalance caused by asymmetry in the disk support structure. Although more study is needed to decipher the exact mechanism, the dependence of the pull-in voltage on stem location suggests a tilting mechanism for disk pull-in. This is not to say, however, that disks with perfectly aligned stems should exhibit infinite pull-in voltages. If tilting were the mechanism for pull-in, then a disk with a perfectly aligned stem still would be susceptible to electrode-to-disk gap variations that compromise the perfect balance of electrostatic forces that might otherwise allow a much higher pull-in voltage.

Perfect stem alignment also does not guarantee high Q. In particular, in addition to misalignment, the finite diameter of the stem also significantly impacts the achievable Q. In particular, because the node at the disk center exists only at a single, infinitesimally small point, and motion still occurs at locations immediately outside that point, the presence of a finite-width stem attempting to restrict that

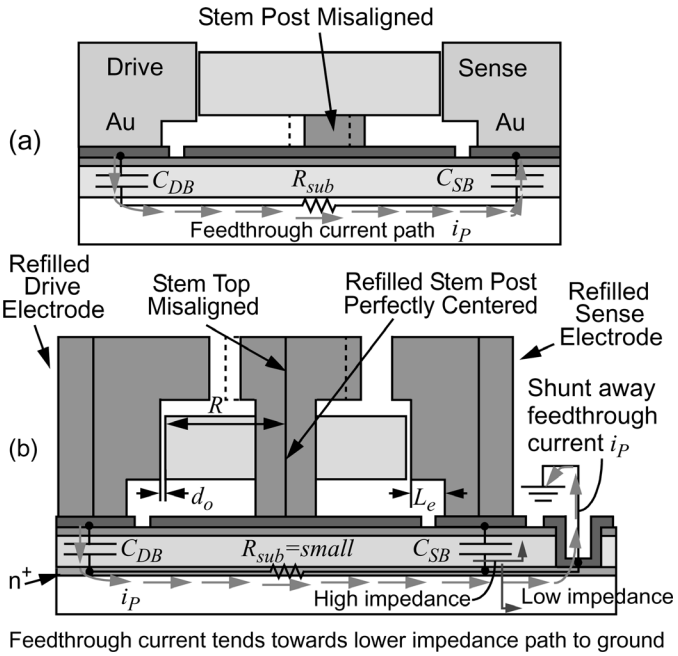

Fig. 6. Comparison between (a) a previous disk process [11] and (b) the new self-aligned disk process, each with the same amount of misalignment. Here, misalignment in (a) leads to stem misalignment, but only stem-top misalignment in (b), which does not lower Q because the stem top sits on a motionless nodal point that never moves during disk vibration, thus causing no added energy loss even considering finite-stem size. In addition, the use of a contacted substrate ground plane in (b) prevents feedthrough current i_p from reaching the output electrode, making resonance detection easier.

motion results in further energy dissipation. Section VII presents actual measurements quantifying the impact of stem diameter on Q.

VI. Self-Aligned Stem Fabrication Process

Given the importance of stem alignment described above, the fabrication process of this work is designed to eliminate the possibility of disk-to-stem misalignment, by simply removing the need for alignment in the first place. In particular, instead of using an anchor mask to first define the stem then another mask aligned to the first to define the disk around the stem, as was done in a previous metal-electrode disk resonator process [11], the present process defines both the stem position and disk edges all in one mask, effectively eliminating the possibility of stem misalignment. An additional difference between this process and the previous one is the inclusion of an electrically accessible substrate ground plane, which proves instrumental in suppressing feedthrough currents to allow clean measurement of gigahertz vibrating disk frequency characteristics. Fig. 6 summarizes the differences between the present self-aligned process and its predecessor.

Fig. 7 presents cross sections and associated scanning electron micrographs (SEM's) summarizing the process flow that achieves self-aligned-stem disk resonators. Right at the outset, the process differs from [11], in that it starts with a heavy phosphorous diffusion to serve as the substrate ground plane mentioned above. This is followed by polysilicon surface micromachining steps similar to those used in the process of [11] up to the point of defining the disk structure. Specifically, a 2-μm thick low pressure chemical vapor deposited (LPCVD) high-temperature oxide (HTO) film is first deposited at 920°C using a $SiCl_2H_4/N_2O$-based recipe over the n^+-doped substrate, followed by a 350 nm-thick film of LPCVD Si_3N_4, and these two layers together serve to isolate devices and interconnects from the conductive silicon substrate. Next, 100 μm $\times$ 100 μm substrate contact trenches are dug by a combination of dry and wet etches through the oxide/nitride isolation layers. Interconnect polysilicon then is deposited via LPCVD to a thickness of 350 nm and $POCl_3$-doped. After patterning this polysilicon layer to form ground planes, interconnects, and substrate contact pads, 800 nm of LPCVD HTO is deposited to act as a sacrificial layer to temporarily support a subsequent structural polysilicon layer during its own deposition and patterning. The structural polysilicon film is deposited 2-μm thick via LPCVD at 588°C, at which temperature a low-stress, fine-grained material is achieved [30]. This film is $POCl_3$-doped, then capped with a 1-μm thick film of HTO that serves as both a hard mask during etching of the structural polysilicon film, and later as a spacer layer to separate the disk from overhanging electrode portions.

Before etching, the structural polysilicon is annealed in N_2 at 1050°C for 1 hour to activate dopants and relieve residual stress—an important step that ensures a high Q structural material. Then, in another substantial deviation from [11], the composite oxide mask/polysilicon layer is patterned in a single mask to define not only the disk structure, but also a 2-μm diameter opening at its center that defines the eventual location of the stem. Here, the oxide hard mask is patterned and plasma etched to the desired device geometries. These patterns then are transferred to the underlying structural polysilicon layer via a high-density inductively coupled plasma (ICP) process, using an SF_6/C_4F_8 chemistry to ensure vertical sidewalls. An LPCVD sidewall sacrificial HTO film then is conformally deposited to a thickness equal to the desired electrode-to-disk gap spacing (e.g., 100 nm) to define the eventual electrode-to-resonator capacitive gap spacing, yielding the cross section of Fig. 7(a) and (a′). Pursuant to eventual refilling of the stem opening, a 6.6-μm thick AZ9260 (Clariant, Somerville, NJ) photoresist (PR) is spun and patterned to expose the stem and the electrode vias, after which the sidewall sacrificial spacer oxide is removed in the stem opening and the underlying bottom sacrificial oxide is etched down to the substrate via a combination of wet and dry etches [c.f., Fig. 7(b) and (b′)]. With exposed stem holes and electrode anchor vias, a subsequent (third) 2-μm LPCVD low-stress polysilicon deposition then not only provides the material for electrodes, but also refills the anchor vias to create very rigid, self-aligned stems [c.f., Fig. 7(c) and (c′)]. This third polysilicon layer is then $POCl_3$-doped, during and after which an oxide phosphorous diffusion barrier is grown to a few hundred nanome-

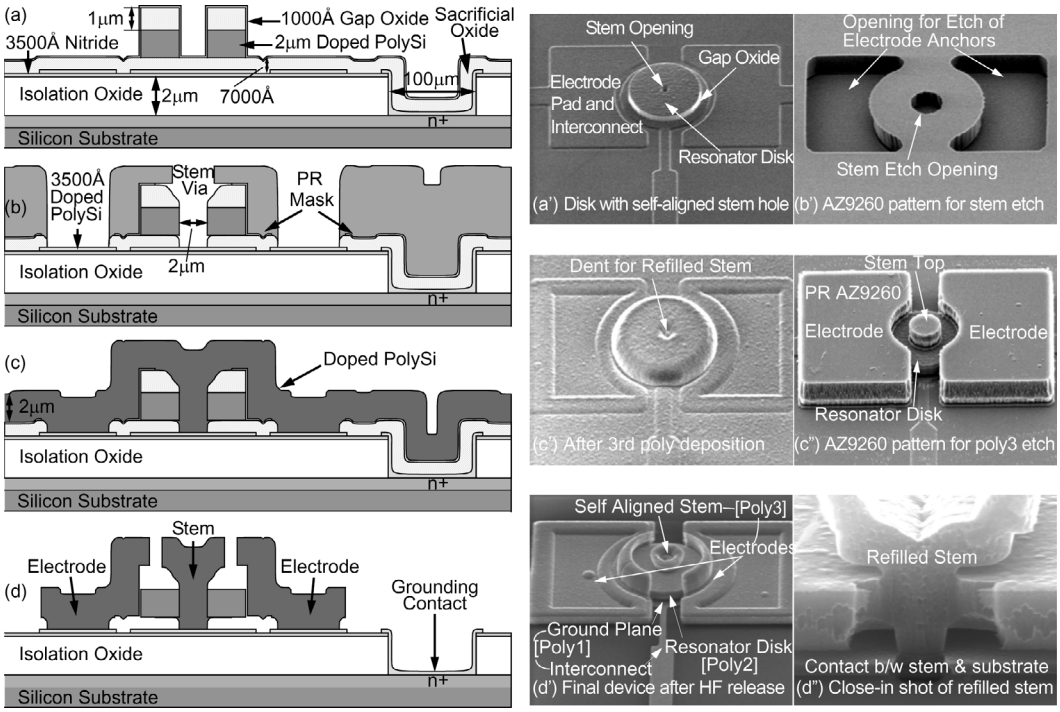

Fig. 7. Fabrication process flow for stem self-aligned, radial-contour-mode disk resonators, featuring a substrate ground plane to suppress parasitic feedthrough. (a)–(d) Cross-sectional diagrams for this process. (a′)–(d″) SEM's at different stages of the process.

ters, which helps to contain the phosphorous during a subsequent annealing step in N_2 at 1050°C for 1 hour. In future renditions of the process, the previous anneal will likely be combined with this one. After annealing, the oxide diffusion barrier is removed in hydrofluoric acid (HF).

To define electrodes, a layer of AZ9260 photoresist then is spun 6.6-μm thick to completely submerge the structural polysilicon topography deep under the quasi-planarized photoresist film. After exposing and developing the photoresist [c.f., Fig. 7(c″)] then patterning the top polysilicon to define stem tops and electrodes, structures are released in 49% concentrated HF to yield the final cross section of Fig. 7(d) and (d′). Fig. 7(d″) shows a close-up cross-sectional SEM visually verifying that the refilled stem is solidly attached to both the underlying substrate and the inner disk sidewalls.

After release, the disk resonators often are also taken through a supercritical CO_2 drying step [31] that increases the yield of testable devices mainly by cleaning their surfaces and removing moisture, and to a lesser degree, by suppressing surface-tension-induced pull-down of devices [32]. It should be noted that the disk resonators of this work are quite stiff, even against tilting, so surface-tension-induced pull-in is normally not a problem here, especially for the smaller disks.

It also should be noted that the ability to anneal these resonators up to 1050°C is an important potential advantage for electrostatically transduced micromechanical resonators over other resonators (e.g., quartz and other piezoelectrics), for which the thermal limit is much smaller. For example, because quartz undergoes a phase transition at 573°C, and it twins at elevated temperatures below 573°C, quartz resonators are generally processed at temperatures no higher than about 300°C. With processing temperatures up to 1050°C, the disk resonators of this work potentially can be cleaner and more stress free than other temperature-limited resonators; if so, two of the major causes of instability in high quality resonators (contamination and stress relief) might be more easily controlled in MEMS technology. As covered in the next subsection, however, whether or not micromechanical resonators can truly capitalize on this potential for high-temperature processing might be dependent upon whether or not low-capacitance integration with transistors is needed and on the method by which such integration is achieved.

A. Integration or Low-Capacitance Merging with Transistor Circuits

The self-aligned lateral disk resonator planar fabrication process described above, together with the ability to specify numerous frequencies via CAD layout, present a low-cost path toward the switchable resonator/filter bank chip described in Section I, using off-chip control circuits. However, if it makes economic sense to integrate or merge in a low-capacitance manner these devices together with integrated circuit transistors, then there already are several approaches to doing this, some of which would require changes to the fabrication sequence described above and some of which require no changes. For example, fabrication sequences that intermix transistor and MEMS process steps to achieve fully integrated MEMS/transistor systems (e.g., the Analog Devices BiMOSII process [33]) would require substantial changes to their process sequences in or-

der to incorporate the above self-aligned disk process. This is not surprising, however, as such intermixed processes generally are nonreceptive to any changes in their process sequences, even relatively small changes (e.g., a change in transistor gate length).

However, more modular integration processes in which the MEMS and transistor process portions (i.e., modules) are kept completely separate, with no intermixing of steps, are much more conducive to process changes in either the MEMS or the transistor modules. To date, however, there is no panacea of modular MEMS/transistor processes, as all of the modular processes demonstrated so far are not perfectly modular, but rather, impose some restrictions on either the transistor or MEMS portions. For example, postcircuit modular processes [34]–[36], where the MEMS module follows the transistor module, are generally restricted by the temperature ceiling of the MEMS module, which is constrained by the need to avoid degrading the underlying transistor circuits. In general, it is the materials and junctions associated with aluminum or copper metallization layers in transistor processes that are most impacted by elevated temperatures. Thus, in a postcircuit process, either the MEMS module must stay below a temperature acceptable to the metallization layers (e.g., $<400°C$) [34], or a nonstandard metal material (e.g., tungsten [35]) that can withstand higher MEMS processing temperatures (e.g., 585°C, for LPCVD polysilicon) must be used. If the latter is acceptable, then the process of [35] should be able to support the self-aligned lateral resonator process of this work, provided the polysilicon is doped in situ during LPCVD deposition, and rapid thermal-annealed (RTA'ed) instead of furnace-annealed, as was done in [35]. If not, and standard metallizations are a must (which is generally the case), then modification to the self-aligned process is required, perhaps using SiGe [36] or low temperature chemical vapor deposited (CVD) nanocrystalline diamond [37] as the MEMS structural material.

Precircuit modular processes, in which the MEMS module precedes the transistor module [38], although generally not amenable to IC-incompatible MEMS processes (e.g., metal MEMS), actually can be quite accommodating to the tiny-gap, lateral resonator process flow of this work. In particular, because the MEMS module comes first, it is not encumbered with temperature limitations, although it must be able to survive the temperatures required for transistor fabrication, which is the case here. In fact, the self-aligned lateral resonator process described above should fit nicely into the process flow of [38], as long as the needed minimum lithographically-determined lateral dimensions are not too small. (The process of [38] might be limited in lithographic resolution because the MEMS structures to be defined are in a trench below the surface of the silicon substrate. This trench then is filled and planarized before transistor processing [38]). However, one possibly more debilitating drawback with most precircuit modular processes, is the short supply of IC foundries willing to accept preprocessed wafers as starting wafers for their processes. It seems that contamination and substrate flatness are the more serious issues for precircuit processes.

In addition to fully planar integration methods, bonding processes, in which transistor circuits and micromechanics are merged by bonding one onto the wafer of the other, are presently undergoing a resurgence [39], [40]. In particular, the advent of more sophisticated aligner-bonder instruments are now making possible much smaller bond pad sizes, which soon may enable wafer-level bonding with bond pad sizes small enough to compete with fully planar processed merging strategies in interface capacitance values. If the bond capacitance can indeed be lowered to this level with acceptable bonding yields, this technology may well be the ultimate in modularity because it allows the combination of virtually any micromechanical device (e.g., even those made in diamond) with any transistor integrated circuit technology.

Fig. 8 presents the cross section of a recently demonstrated process that combines micromechanics with transistor circuits using a microplatform bond and transfer approach [40]. In this process, micromechanics are first fabricated onto microplatforms, which are themselves released and suspended over their MEMS carrier wafer by temporary tethers. The suspended microplatforms then are flipped and bonded to receiving bond pads on a transistor wafer, then physically torn from the MEMS carrier wafer by breaking the suspending tethers. This bonded platform technology allows low-capacitance, single-chip, merging of MEMS and transistors with several key advantages: It is truly modular, requiring no compromises in either the MEMS or transistor modules. It attempts to minimize Q-degrading anchor losses experienced by previous bonding-based methods [39] by bonding platforms housing resonators, instead of directly bonding the anchors of resonators. It constitutes not only a wafer-scale batch approach, but also a repeatable approach in which a step-and-repeat procedure can be used to allow a single MEMS wafer to service several transistor wafers. The self-aligned lateral resonator process described above might simply incorporate the process of Fig. 7, with few changes, except for the addition of the needed metal bonding layers.

VII. Experimental Results

Several self-aligned, radial-contour mode micromechanical disk resonators with frequencies from 150 MHz to 1.156 GHz were designed using the methods of Section II, then fabricated using the process flow described above and shown in Fig. 7. Table I summarizes the dimensions used for each design along with measured and predicted performance data to be addressed later.

A custom-built vacuum chamber with printed circuit board support and electrical feedthroughs allowing coaxial and DC connections to external instrumentation, was used to characterize all resonators. In this apparatus, dies containing devices-under-test were epoxied to a custom-built printed circuit board (PCB) chip carrier containing

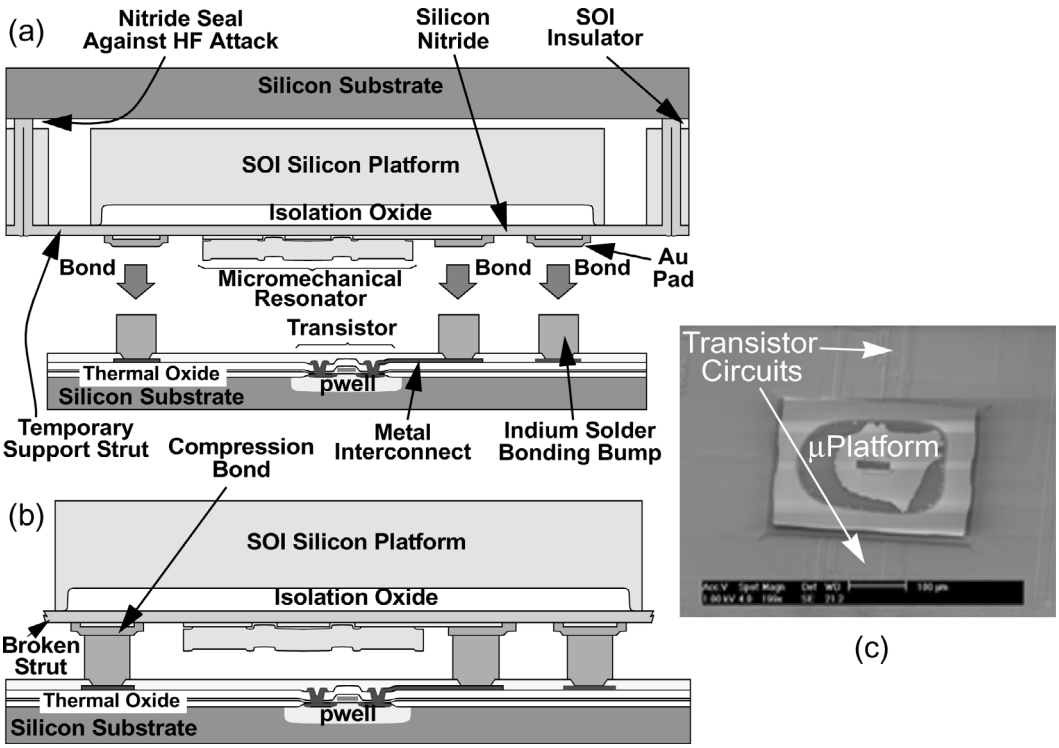

Fig. 8. Illustration of the procedure for achieving a combined MEMS/transistor chip via the described flip-bond-and-tear process [40]. (a) Bonding, (b) final cross-section, (c) SEM of a bonded microplatform over CMOS circuits.

highly-isolated, coplanar waveguide (CPW) ports serving as drive and sense ports to be bonded to the resonator's I/O ports on chip. For vacuum measurements, a turbo molecular pump was used to evacuate the chamber to pressures on the order of 50 μtorr (to remove viscous gas damping mechanisms) before testing devices.

As mentioned in Section I, micromechanical resonators often exhibit port-to-port impedances much larger than conventional macroscopic devices making them more vulnerable to parasitics. For example, if the series resistance of a micromechanical resonator is large enough, currents feeding through port-to-port parasitic feedthrough capacitance might easily swamp the motional current due to the resonator itself. This is not perceived to be as much of a problem when the resonators are used in single-chip, fully integrated systems in which the resonators are integrated directly alongside transistors with no need for large (100-μm square) bond pads, so with very little port-to-port parasitic capacitance; and with no need for 50 Ω impedance matching, since most on-chip transistor circuits are actually more comfortable at higher impedances. (For example, power hungry buffers often must be added to on-chip CMOS transistor circuits just to drive the 50 Ω of off-chip components [41].) However, difficulties can arise when these devices must interface directly with off-chip, macroscopic components in which bond wires must connect large bond pads to coax, which then must connect to 50 Ω measurement instrumentation. In this case, bond pads and bond wires contribute substantially larger port-to-port feedthrough capacitance, making masking of motional current by parasitic feedthrough a significant problem [42]. In addition, the large impedance of the disk resonator forms a voltage divider with the 50 Ω input resistance typical of measurement instrumentation (e.g., a network analyzer or a spectrum analyzer), and this greatly reduces the fraction of the (already small) power of the resonator device actually delivered to the measurement instrument. This latter effect is responsible for losses seen in network analyzer plots obtained using the two-port measurement scheme of Fig. 2, such as that of Fig. 11(b), to be discussed later. In other words, this loss is due to impedance-mismatching, not due to the resonator device under test itself.

The parameters of major interest for the present resonator devices are resonance frequency f_o, quality factor Q, and series motional resistance R_x, all of which can be obtained from the frequency domain transfer characteristic obtained by the network analyzer in the two-port measurement set-up in Fig. 2. The resonance frequency, of course, can be obtained straight from the network analyzer plot. The Q can be obtained via the expression:

$$Q = \frac{f_o}{BW_{3dB}}, \tag{31}$$

where BW_{3dB} is the 3 dB bandwidth of the resonator, and where Q loading is neglected as the series resistance of the micromechanical device is many times larger than the interconnect, coaxial, and input port resistance (50 Ω), combined, of the measurement setup. In fact, resonator measurements are made without any attempt to match the resonator impedance to the instrument impedance, despite impedance-mismatch losses, in order to suppress Q

TABLE I
SELF-ALIGNED DISK RESONATOR DESIGN AND PERFORMANCE SUMMARY.

Row No.	Parameter	Source	Target frequency: Actual fabricated device: 151.3 MHz (1st mode)	274 MHz (1st mode)	734.6 MHz (2nd mode)	1.156 GHz (3rd mode)	Theoretical: 734 MHz [calc] (2nd mode)	1.15 GHz [calc] (3rd mode)	Unit
			Designed/Given						
1	Disk diameter, $2R_{disk}$	layout	36	20	20	20	20	20	μm
2	Disk thickness, t	layout	2.1	2.1	2.1	2.1	**10.0**	**10.0**	μm
3	Stem diameter, $2R_{stem}$	layout	2.0	1.6	1.6	1.6	1.6	1.6	μm
4	I/O electrode width, W_e	layout	53.4	29	30.5	30.5	30.5	30.5	μm
5	Electrode-to-resonator gap, d	measured	870	680	680	680	**300**	**300**	Å
6	Density, ρ	[12]	2300	2300	2300	2300	2300	2300	kg/m^3
7	Young's modulus, E	measured	150	150	150	150	150	150	GPa
8	Poisson ratio, σ	[30]	0.226	0.226	0.226	0.226	0.226	0.226	—
9	Frequency scalor, κ	(12)	0.342	0.342	0.342	0.342	0.342	0.342	MHz/μm
10	Mode-dependent factor, α	(12)	1	1	2.64	4.21	2.64	4.21	—
11	h	(8)	0.115	0.207	0.557	0.876	0.557	0.876	1/μm
12	Force/dependent ratio, A	(6)	0.0111	0.0259	0.002	0.00017	—	—	μm^2
13	RF input amplitude, v_{RF}	measured	1	2.24	3.162	3.162	—	—	V
14	LO carrier amplitude, v_{LO}	measured	6	8.91	7.943	7.943	—	—	V
15	V_P Used in measurement, V_{Pm}	measured	6	30.54	10.5	10.5	**40**	**40**	V
16	Resonator Mass, m_{re}	(24)	3.83×10^{-12}	1.08×10^{-12}	1.43×10^{-12}	1.43×10^{-12}	6.77×10^{-12}	7.02×10^{-12}	kg
		FEA (24)	3.79×10^{-12}	1.11×10^{-12}	1.49×10^{-12}	1.49×10^{-12}	6.92×10^{-12}	7.15×10^{-12}	
17	Resonator stiffness, k_{re}	(25)	3.52	3.19	30.4	75.5	144.0	367.1	MN/m
		FEA (25)	3.43	3.29	31.7	78.6	147.2	373.1	
18	Damping factor, c_{re}	(25)	3.01×10^{-7}	2.07×10^{-7}	8.34×10^{-7}	3.87×10^{-6}	3.95×10^{-6}	9.40×10^{-6}	kg/s
		FEA (26)	2.93×10^{-7}	2.14×10^{-7}	8.70×10^{-7}	4.02×10^{-6}	4.04×10^{-6}	9.55×10^{-6}	
			Performance						
19	Measured power output, P_o	vacuum	−75.66	−50.47	−68.81	−82.22	—	—	dBm
		air	−78.12	−51.76	−73.2	−82.34	—	—	
20	Measured quality factor, Q	vacuum	12,289	8950	7890	2683	**7900**	**5100**	—
		air	9316	7500	5160	2655	—	—	
21	Vib. ampltd, $\Re(R_{disk}, \theta)$	(7)	7.3	32.3	3.9	0.41	—	—	Å
22	Fundamental frequency, f_o	measured	151.3	273	274.5	274.5	—	—	MHz
		ANSYS 6.0	152.4	274.8	274.8	274.8	274.8	274.8	
		(10, (11)	152.4	274	274	274	274	274	
23	2nd Mode frequency, f_{02}	measured	405.2	733	734.6	734.6	—	—	MHz
		ANSYS 6.0	402.4	725.9	725.9	725.9	725.9	725.9	
		(10), (11)	402.0	726	726	726	726	726	
24	3rd Mode frequency, f_{o3}	measured	645.0	1140	1156.0	1156.0	—	—	MHz
		ANSYS 6.0	641.9	1155.9	1155.9	1155.9	1155.9	1155.9	
		(10), (11)	640.0	1151	1151	1151	1151	1151	
25	4th Mode frequency, f_{o4}	measured	872	—	—	—	—	—	MHz
		ANSYS 6.0	873.1	1572	1572	1572	1572	1572	
		(10), (11)	875.3	1575	1575	1575	1575	1575	
26	Series resistance, R_x	meas. (A5)	479.667	17.24	521.4	2441.9	—	—	kΩ
		FEA (28)	466.990	16.96	542.1	2546.5	0.307	0.754	
		(28)	479.526	16.39	519.7	2451.5	0.300	0.742	
27	Inductance, L_x	meas. (A6)	6.19	0.896	0.891	0.902	—	—	H
		FEA (28)	6.04	0.0880	0.928	0.944	5.25×10^{-4}	5.31×10^{-4}	
		(28)	6.20	0.0854	0.889	0.906	5.13×10^{-4}	5.23×10^{-4}	
28	Capacitance, C_x	meas. (A7)	1.79×10^{-19}	3.77×10^{-18}	5.27×10^{-20}	2.10×10^{-20}	—	—	F
		FEA (28)	1.83×10^{-19}	3.83×10^{-18}	5.06×10^{-20}	2.01×10^{-20}	8.96×10^{-17}	3.60×10^{-17}	
		(28)	1.78×10^{-19}	3.97×10^{-18}	5.28×10^{-20}	2.09×10^{-20}	9.16×10^{-17}	3.66×10^{-17}	

loading, and hence, obtain a very accurate reading of the actual resonator Q.

The series motional resistance $R_{x[Measured]}$ measured using a direct two-port measurement scheme, such as shown in Fig. 2, can be obtained via the expression:

$$R_{x[Measured]} = R_L \left(10^{-(A/20)} - 1\right) - R_S - R_p, \tag{32}$$

where A is the transmission gain in decibels at the peak of the measured frequency characteristic, R_S and R_L are the source and load resistance of the network analyzer (both 50 Ω), and R_p is the total parasitic resistance in series with the device under test.

In most cases, a direct two-port measurement setup, such as shown in Fig. 2, was sufficient to obtain frequency and Q data, albeit with up to −62 dB of transmission loss, caused not by the resonator device but by the aforementioned large mismatch between the resonator impedance and the 50 Ω network analyzer test-port impedance. The use of an electrically accessible substrate ground plane to shunt feedthrough currents away from the output electrode proved instrumental in allowing direct two-port measurement of devices. As shown in the measured feedthrough versus frequency plots of Fig. 9, more than 10 dB of feedthrough suppression was achieved at frequencies below 1 GHz via substrate grounding.

A. Mixing Measurement Setup

When impedance mismatches made direct two-port measurement impossible, despite substrate grounding, a mixing-based measurement setup shown in Fig. 10 was used that suppressed parasitic feedthrough by moving motional currents away from them in the frequency domain [43], [44], allowing adequate measurement of devices. In this scheme, which is more fully covered in [43], a device is driven by off-resonance signals (an RF signal v_{RF} and a carrier signal v_{LO}) which mix through capacitive trans-

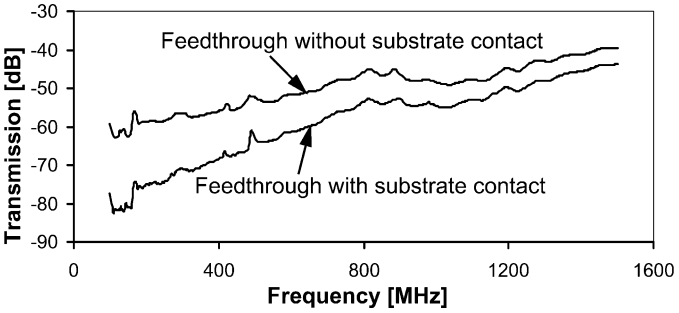

Fig. 9. Measured feedthrough versus frequency for devices with and without an electrically accessible substrate ground plane.

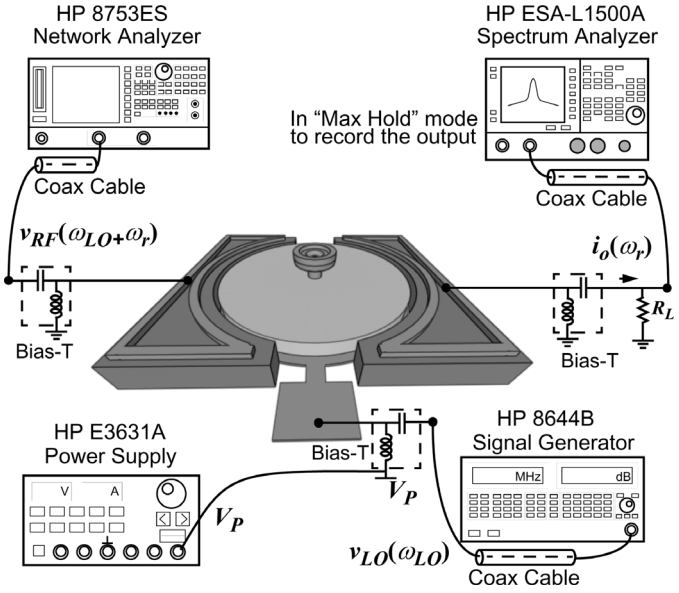

Fig. 10. Schematic illustrating the mixing measurement scheme, showing detailed connections for bias tees, signal and bias generators, and measurement instrumentation.

ducer nonlinearity to generate a force at their difference frequency that, if equal to the resonance frequency f_o, then drives the resonator into vibration. Because none of the input voltage signals is at the resonance frequency, no direct feedthrough is expected at this frequency, and output currents at this frequency are free from parasitic interference. Ideally, only noise limits the detectable range.

As shown in Fig. 10, this mixing measurement scheme requires a very specific input arrangement, including: a carrier signal v_{LO} with frequency f_{LO} (generated by an HP 8644B signal generator, Hewlett-Packard (Agilent), Palo Alto, CA) not equal to the resonance frequency f_o; a DC-bias voltage V_P (generated by an HP E3631A power supply, Hewlett-Packard (Agilent)) applied to the resonator disk; and an RF signal v_{RF} with frequency $f_{RF} = f_o + f_{LO}$ (generated by an HP 8753ES network analyzer, Hewlett-Packard (Agilent)), also not equal to f_o, applied to the drive electrode. Even though none of the applied signals used to excite the resonator is within the passband of micromechanical resonator, a force component at resonance still arises at the input due to quadratic nonlinearity in the voltage-force capacitive input transducer, given by:

$$\begin{aligned} F_i &= \frac{1}{2}\left(V_P + v_{LO} - v_{RF}\right)^2 \left(\frac{\partial C_1}{\partial r}\right) \\ &= \cdots - v_{LO} v_{RF} \left(\frac{\partial C_1}{\partial r}\right) + \ldots \\ &= \underbrace{\cdots - \frac{1}{2} V_{LO} V_{RF} \left(\frac{\partial C_1}{\partial r}\right) \cos\left(\omega_{RF} - \omega_{LO}\right) t}_{F_{mix}} + \ldots, \end{aligned} \tag{33}$$

where $v_{RF} = V_{RF} \cos \omega_{RF} t$, $v_{LO} = V_{LO} \cos \omega_{LO} t$, and where the mixed component of interest F_{mix} at $\omega_o = \omega_{RF} - \omega_{LO}$ has been singled out in the last expression.

Once forced into resonance vibration by the above force component at ω_o, the resonator under test outputs a motional current as usual, given in terms of force F_{mix} (and in phasor form) by:

$$I_o = \omega_o V_P \left(\frac{\partial C_2}{\partial r}\right) \frac{Q}{k_{re}} F_{mix}. \tag{34}$$

This output current is monitored in the IF range (i.e., the resonator bandpass range, around f_o) by a spectrum analyzer in MAX HOLD mode while the device is driven by an RF signal v_{RF} swept around $f_{RF} = f_{LO} + f_o$, with a local oscillator voltage v_{LO} applied as in Fig. 10. In MAX HOLD mode, the spectrum analyzer retains the highest measured value seen at the frequency of the signal being measured. Under this measurement mode, by sweeping the input frequency over one range (e.g., the RF range) while measuring over another (e.g., the IF range), a spectrum analyzer can obtain a transmission spectrum over a frequency range different from the input frequency range. Although several sweeps are usually required to obtain sufficiently smooth spectra, this measurement approach can yield transmission spectra as good as attainable via a network analyzer, but without the network analyzer's constraint for identical input and output frequency ranges. Such a MAX HOLD measurement mode is obviously ideal for the mixing-measurement method.

To verify the validity of the mixing measurement technique for characterizing electrostatically transduced resonators, Fig. 11 compares the frequency characteristics of a 20-μm diameter fundamental mode disk resonator measured using both the mixing method of Fig. 10 and the traditional two-port setup of Fig. 2. Here, excellent agreement is seen for resonance frequency, quality factor, and extracted motional resistance. In fact, the mixing measurement technique actually provides the more accurate numbers between the two. In particular, due to a higher feedthrough noise level that distorts its measured resonance peak, the two-port measurement yields a 6% lower extracted Q value and a 5% smaller extracted series motional resistance than the mixing technique. By suppressing feedthrough, the mixing technique allows measurement of a substantially cleaner resonance spectrum, thus providing more accurate data with which to characterize the intrinsic performance of micromechanical resonator devices,

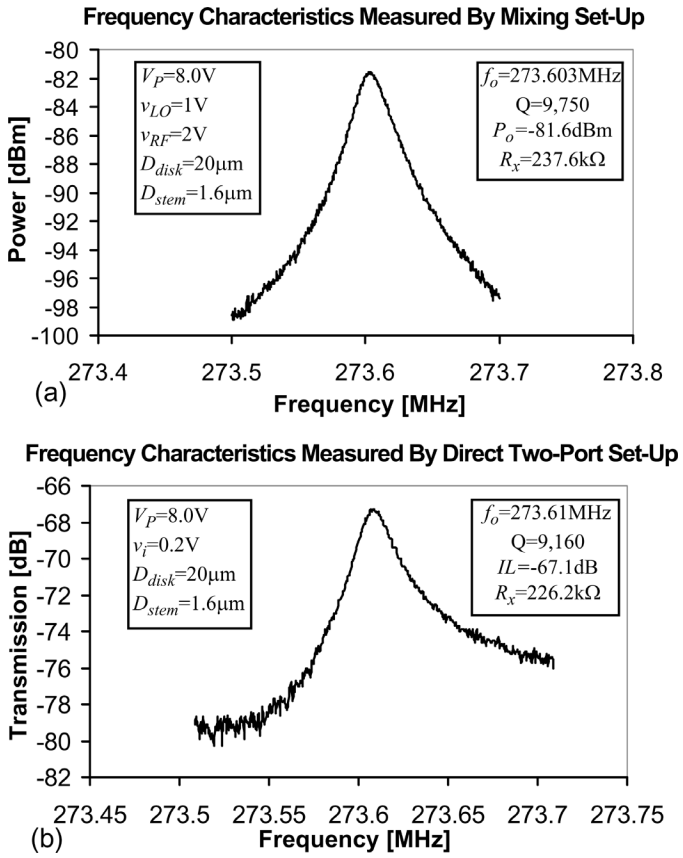

Fig. 11. Comparison between frequency characteristics (a) for a 20-μm diameter disk resonator operating in its fundamental radial-contour mode measured using the mixing setup shown in Fig. 10; and (b) for the same device measured by the direct two-port setup shown in Fig. 2, demonstrating good agreement in terms of measured resonance frequency f_0, Q and extracted motional impedance R_x.

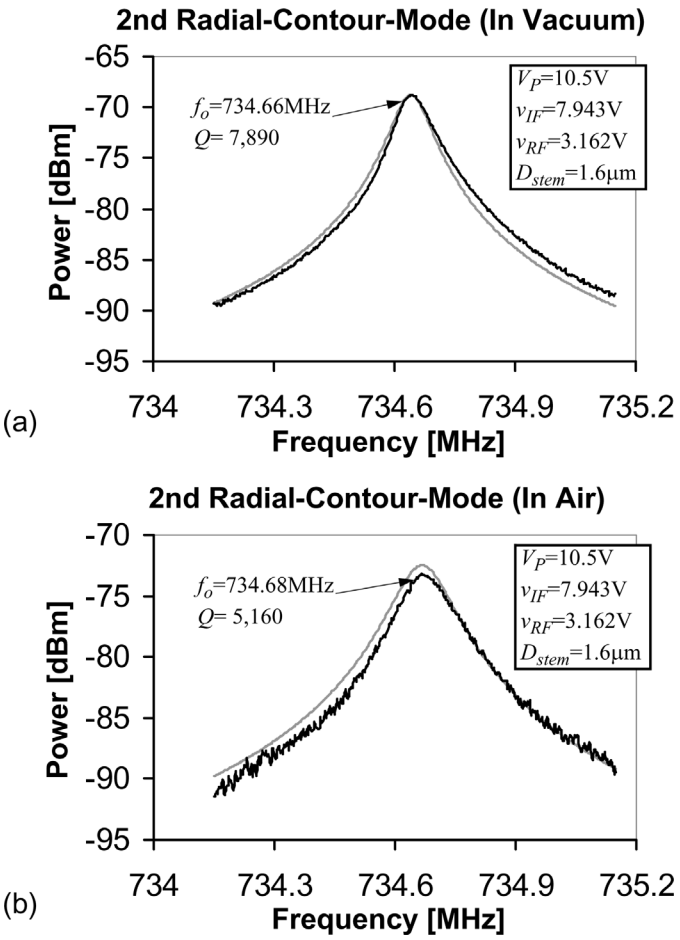

Fig. 12. Measured (dark lines) and predicted (light lines) frequency characteristics for a 734.6-MHz, 2nd radial-contour mode, 1.6-μm diameter stem, 20-μm diameter, disk resonator measured in (a) vacuum and (b) air, using the mixing setup shown in Fig. 10.

especially ones designed to operate at higher frequencies, for which feedthrough is more problematic in off-chip test setups.

Whether data is obtained using the direct or the mixing measurement schemes, neither of which attempts to match device impedances to that of measurement instruments, losses due to impedance mismatching are expected. Again, these losses are impedance-match derived and are not indicative of actual device loss. By their sheer high Q, it should be obvious that the devices should exhibit very little loss when used in properly matched filters, as has already been demonstrated in [16] and [45].

Figs. 12 and 13 present frequency spectra measured using the mixing setup of Fig. 10 for the 20-μm diameter device with 1.6-μm diameter stem operating in its second radial contour mode at 734.6 MHz, showing a Q of 7,890 in vacuum and 5,160 in air; and in its third radial contour mode at 1.156 GHz with Q's of 2,683 and 2,655 in vacuum and air, respectively. (It should be noted that, due to impedance mismatching, the peak height in the latter measurement is somewhat small, so the extracted Q probably undershoots the actual value by a significant amount.) Both measurements verify the prediction of Section IV that the Q's of high stiffness, high-frequency devices should remain high whether operated in vacuum or at atmospheric pressure. In addition to measured spectra, theoretical curves simulated using equivalent circuits based on the formulations of Section III are included in the plots, verifying the accuracy of the models. Table I contains the equivalent circuit element values and presents further comparisons of measured and predicted frequency data, showing good agreement. The Appendix provides details on the exact procedure used to extract equivalent circuit-element values from mixing measurement data.

Although comprehensive aging and drift testing have not been conducted yet, it should be mentioned that the Q and f_0 of devices run continuously in the open laboratory environment for several days were at least stable to better than 50 ppm, with the observed frequency changes fully accounted for by temperature variations in the lab. However, devices measured after storage under laboratory air for several months showed a 2–4X reduction in Q and a total fractional frequency variation in the range of 100–1000 ppm. From previous work [46], such storage-related variations most probably are caused by surface contamination (including both particles and moisture). For this reason, although vacuum packaging may not be required

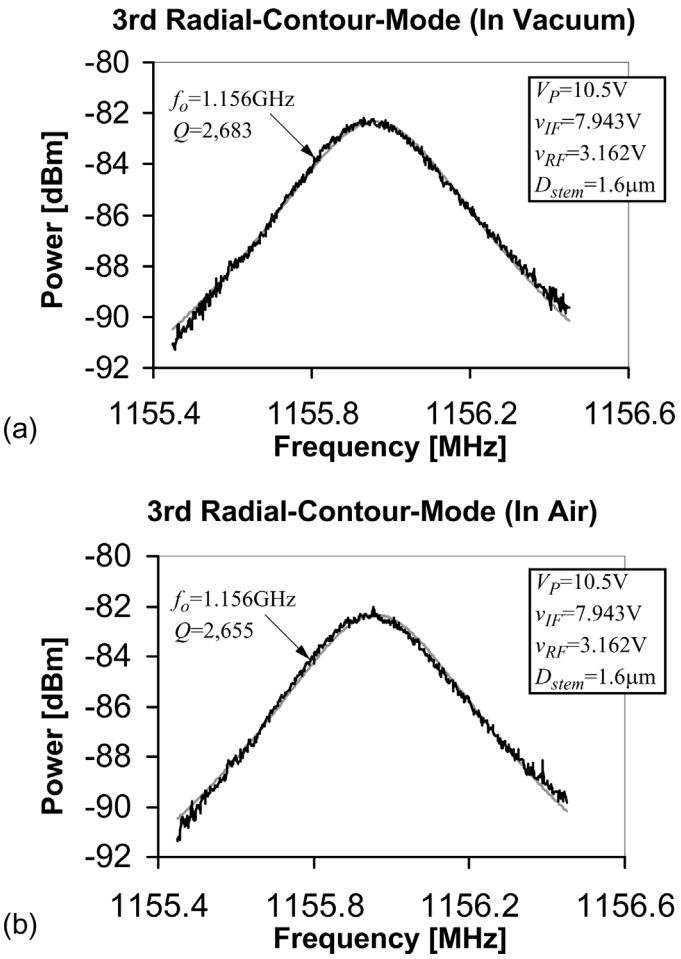

Fig. 13. Measured (dark lines) and predicted (light lines) frequency characteristics for a 1.156-GHz, 3rd radial-contour mode, 1.6-μm diameter stem, 20-μm diameter, disk resonator measured in (a) vacuum and (b) air, using the mixing setup shown in Fig. 10.

as stated above, hermetic packaging will likely be needed still to maintain high Q and frequency stability in practical applications.

B. Q and Frequency Versus Pressure

To further characterize the pressure dependence of micromechanical disk resonators, Fig. 14 presents a plot of Q and frequency versus pressure for a 20-μm diameter disk resonator operating in its fundamental radial-contour mode of about 273.6 MHz over a 200 μTorr to atmospheric pressure ($\sim$760 Torr) range, all done in a sealed chamber with the temperature set at 300 K by a K-20 temperature controller (MMR Technologies, Mountain View, CA). As shown, the Q remains higher than 9,000 all the way up to 100 Torr, and it retains a value of 7,500 even at atmospheric pressure, which is still plenty for communications applications. Thus, vacuum is not needed to attain Q's suitable for present-day applications—a fact that should reduce the cost of packaging for potential products based on these devices, although at least hermetic packaging will likely be required still to prevent contamination-derived instabilities and Q losses.

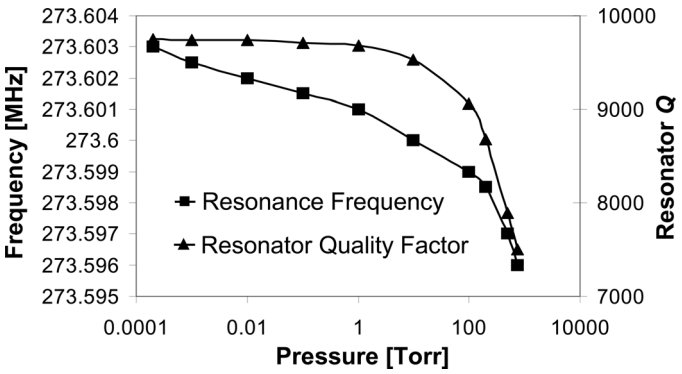

Fig. 14. Measured Q and center frequency versus pressure, for a 20-μm diameter, disk resonator operating in its fundamental radial-contour mode at 300 K.

From Fig. 14, in addition to Q changes, the frequency of the disk resonators also varies with pressure, decreasing by -25.5 ppm over the measurement pressure range. In previous macroscopic resonators, frequency changes due to pressure variations arose from three basic mechanisms [47]: the effect of hydrostatic pressure on the elastic modulus, which generally leads to a linear increase in frequency with pressure; the complex shear impedance of the gas, especially its reactive impedance component, which generally leads to a linear decrease in frequency with the square root of pressure; and/or sorption of gas, for which frequency generally decreases with increasing pressure. For quartz resonators, the first mechanism is often dominant, so the resonance frequencies of quartz devices generally increase with pressure. As seen in Fig. 14, however, the opposite seems to be true for the micromechanical disk resonators of this work, leaving the latter two mechanisms as likely candidates for mechanisms. More detailed study is needed to decipher which, if any of these, is the dominant mechanism.

C. Stem Size

To verify the impact of stem size on disk resonator Q predicted in Section II, Fig. 15 summarizes measured fundamental mode spectra for self-aligned, 36-μm diameter disk resonators with stem diameters ranging from 1.6 μm to 4.0 μm. Here, an almost 7X higher Q is seen for the 1.6-μm diameter stem disk versus its 4.0-μm diameter stem counterpart, all consistent with a mechanism in which restriction of motion at points farther from the disk center leads to increased acoustic energy loss.

If such a mechanism were indeed at work, then resonators with perfectly centered stems operating in higher modes should suffer Q loss even more than those operating in the fundamental mode because their high-velocity points are closer to the stem edges. This is illustrated by Fig. 16, which presents measured second-mode spectra for self-aligned 36-μm diameter disk resonators with stem diameters ranging from 1.6 μm to 2.0 μm. The Q's of these peaks are clearly lower than those of the corresponding ones in Fig. 15. Evidently, for the pure polysilicon disk

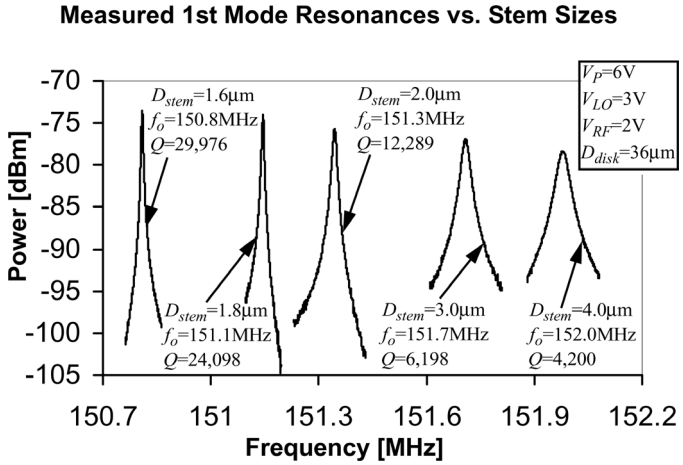

Fig. 15. Frequency characteristics for fundamental radial-contour mode, 36-μm diameter, disk resonators with self-aligned stem diameters varying from 1.6 μm to 4.0 μm, measured using the mixing scheme shown in Fig. 10.

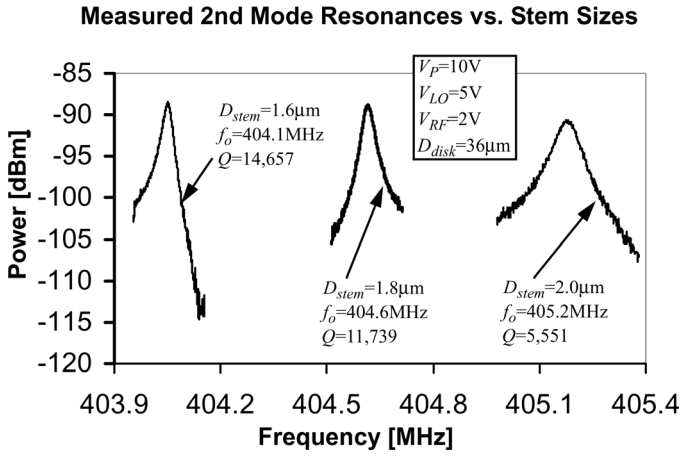

Fig. 16. Frequency characteristics for 36-μm diameter disk resonators operating in the 2nd radial-contour mode with self-aligned stem diameters varying from 1.6 μm to 2.0 μm, measured using the mixing scheme shown in Fig. 10.

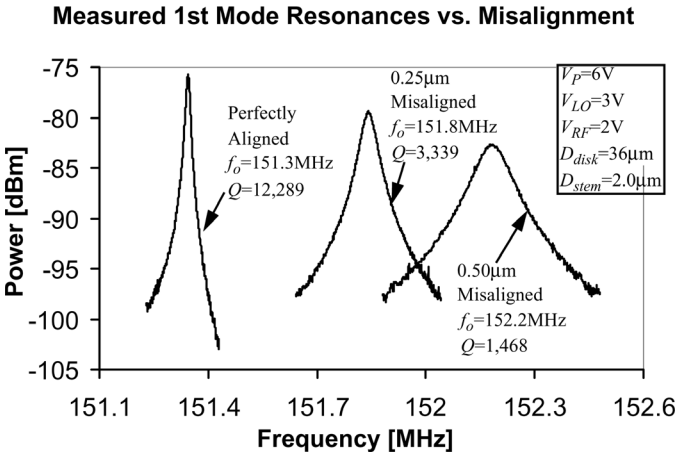

Fig. 17. Frequency characteristics for 36-μm diameter disk resonators with progressively larger misalignments of their 2-μm diameter stems, operating in the fundamental radial-contour mode and measured using the mixing scheme shown in Fig. 10.

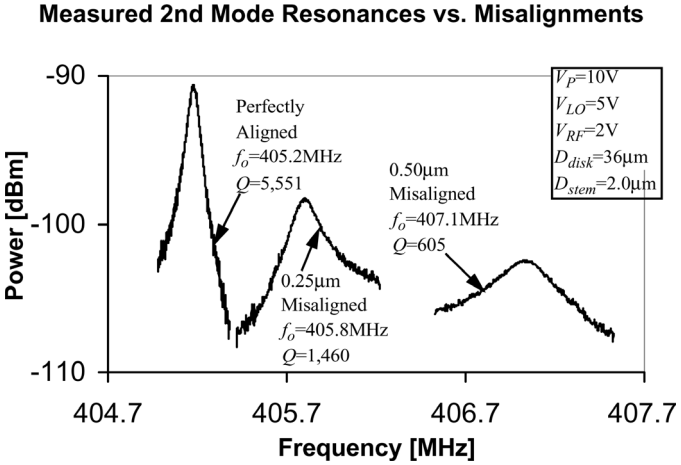

Fig. 18. Frequency characteristics for 36-μm diameter disk resonators with progressively larger misalignments of their 2-μm diameter stems, operating in the 2nd radial-contour mode and measured using the mixing scheme shown in Fig. 10.

resonators of this work, high Q at high frequency is best achieved with thinner stems.

In addition, the rate of Q reduction as stem size increases seems to be similar for fundamental and higher mode devices. For example, in Fig. 16, the use of a 2.0-μm diameter stem versus 1.6-μm diameter in a second-mode resonator introduces a 2.64X reduction in Q, which is only slightly greater than the 2.44X reduction for the fundamental-mode data of Fig. 15.

D. Stem Misalignment

To experimentally investigate the impact of stem misalignment on disk resonator performance and verify predictions made in Section V, disk designs with stems purposely misaligned in CAD layout also were fabricated using the process sequence of Section VI. Figs. 17–19 present measured first, second, and third mode spectra, for several 36-μm diameter disk resonators suspended by 2-μm diameter stems designed with progressively larger misalignments. As shown, regardless of mode, the resonance frequency of these resonators become progressively larger as their stem misalignments are increased. Unfortunately, these increases in frequency are accompanied by dramatic reductions in Q. As shown in these figures, a 0.25 μm (about 1.4% of the disk radius) stem misalignment reduced the resonator Q's by 3.7X, 3.8X, and 5.2X, for the first, second, and third modes, respectively. Stems misaligned by 0.5 μm fared even worse in terms of Q for the first and second modes, and for the third mode, designed stem misalignments greater than 0.25 μm seem to reduce the Q to the point of rendering the device immeasurable. That reductions in Q become larger as the mode number increases is reasonable because the higher the radial mode, the closer the high-velocity points (i.e., rings) to the disk center, and the greater the likelihood that the misaligned stem will couple the disk vibration to the substrate, thus

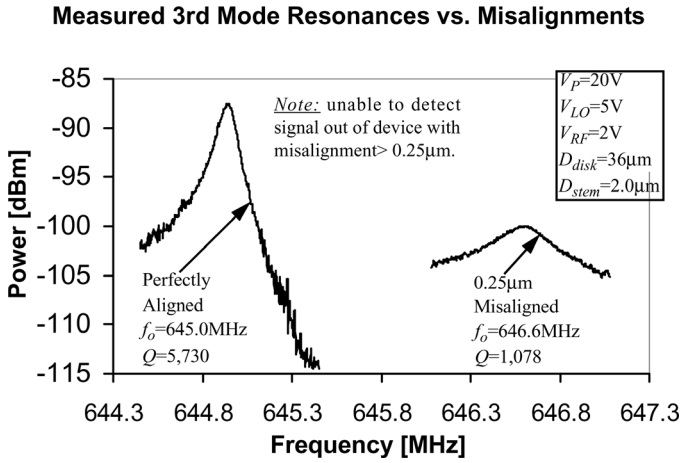

Fig. 19. Frequency characteristics for 36-μm diameter disk resonators with progressively larger misalignments of their 2-μm diameter stems, operating in the 3rd radial-contour mode and measured using the mixing scheme shown in Fig. 10.

losing energy to the substrate and degrading the overall resonator Q.

Given the above, it then should hold that as the disk diameter becomes smaller, Q reductions due to stem misalignment should become even worse. Fig. 20 verifies this with measured frequency characteristics for several 20-μm diameter disk resonators, clearly showing that even the smallest designed stem misalignment of 0.1 μm (1% of the disk radius) reduces the Q of the first and second modes by 4.8X and 8.05X, respectively. Stem misalignments greater than 0.1 μm actually preclude measurement of the first and second modes. No data is reported for the third mode simply because the Q could not be measured even for the minimum designed misalignment of 0.1 μm.

As mentioned in Section V, if disk pull-in occurs by tilting of the disk, the pull-in voltage for a stem-misaligned disk should be smaller than that of one with a self-aligned (i.e., perfectly aligned) stem. Experimentally, pull-in voltages on the order of 40 V for devices with perfectly centered self-aligned stems are routinely measured. However, devices with stems misaligned by 0.5 μm exhibit 3–4X smaller pull-in voltages, suggesting that perhaps tilting might indeed be the mechanism for pull-in of the disk to its electrodes. However, a more detailed study is needed to conclusively state this. Whatever the mechanism for pull-in, the introduction of a dielectric layer (such as silicon nitride) between resonator and electrode is a proven method for preventing catastrophic destruction when pull-in occurs.

E. Temperature Dependence

To verify the resonance frequency temperature coefficient predictions of Section II-D, modifications were made to the custom-built vacuum chamber to allow insertion of an MMR Technologies temperature-controllable cantilever, enabling measurement of the temperature dependence of resonator center frequencies under vacuum en-

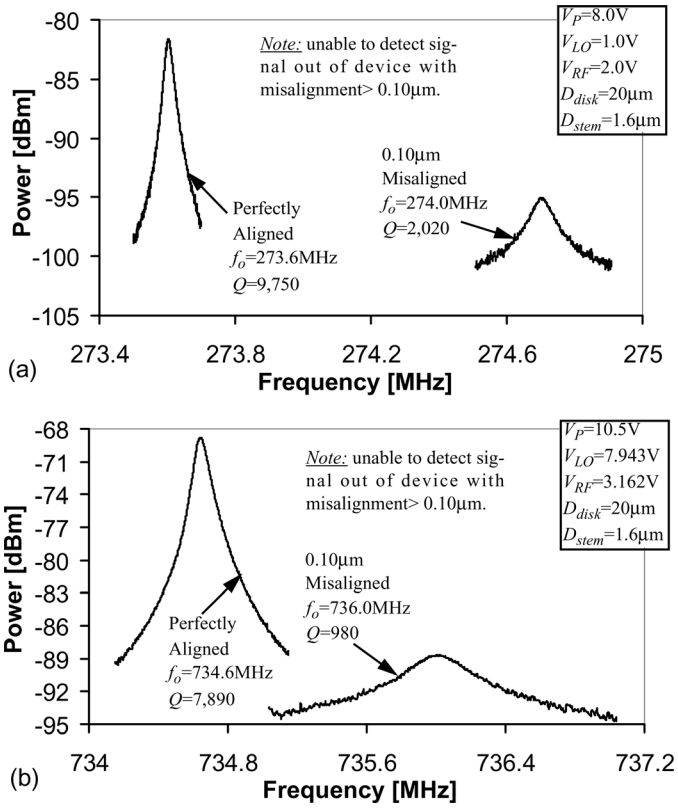

Fig. 20. Frequency characteristics for 20-μm diameter disk resonators with progressively larger misalignments of their 1.6-μm diameter stems, operating in the (a) 1st and (b) 2nd radial-contour modes, respectively, measured using the mixing scheme shown in Fig. 10.

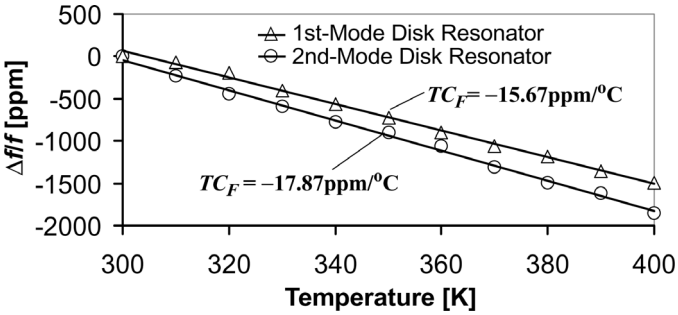

Fig. 21. Measured fractional frequency change versus temperature for 1st and 2nd radial-contour mode, 22-μm diameter, disk resonators.

vironments. Fig. 21 presents measured plots of fractional frequency change versus temperature for a 22-μm diameter disk resonator fabricated using the self-aligned process of Fig. 7 and operated in its fundamental and second modes, in which an expected decrease in frequency with temperature (due to a negative Young's modulus temperature coefficient) is observed. The uncompensated temperature coefficients TC_f's of −15.67 ppm/°C and −17.87 ppm/°C for the fundamental and second modes, respectively, are consistent with the prediction of −22.6 ppm/°C for a 22-μm diameter disk using (19) and are better than that of AlN FBAR technology, which is typically in the range of −25 ppm/°C. These measured temperature coefficients also are comparable to the −16 ppm/°C measured for a

disk resonator with metal electrodes [11], proving at least for these designs that variations in electrode-to-resonator gap with temperature do not significantly affect the overall temperature dependency.

Although sufficient for front-end RF preselect and image-reject filter applications, the measured TC_f's are not adequate for oscillator specifications. The uncompensated temperature coefficient could be further reduced by several different methods, including micro oven stabilization [48], and perhaps even electrical stiffness compensation [13], provided the right design dimensions (e.g., very small electrode-to-resonator gaps) can be realized to raise the electrical stiffness much higher than presently exhibited.

F. Measurement Versus Theory

Along with many of the measured parameters, Table I also provides direct comparisons with numbers obtained by analytical calculation using the formulations developed in previous sections, and by finite-element simulation using ANSYS 6.0, where possible. In particular, although finite-element modal analyses easily obtain the modal resonance frequencies for each resonator design, there are no existing simulation packages capable of correctly predicting the Q of these disk resonators, which are limited more by anchor losses than by internal damping, viscous gas damping [26], or thermoelastic damping [49]. Nor are there yet analytical formulations of any great use for the case of the disk resonator. Thus, the Q data in Table I is purely experimental.

However, the series motional resistance R_x can be obtained analytically via (29), and numerically via a combination of ANSYS simulation and summation. To obtain R_x by numerical simulation, the equivalent mass on the perimeter of the disk can be obtained by first extracting displacements for all meshed nodal elements, $\Re(r,\theta)$, from finite element (FE) simulation, then evaluating the expression

$$m_{re[FE]} = \frac{\sum\limits_{Elements} dm \times [\Re(r,\theta)]^2}{[\Re(R_{disk},\theta)]^2}, \qquad (35)$$

where dm and $\Re(r,\theta)$ are the mass and displacement, respectively, for each meshed nodal element, and $\Re(R_{disk},\theta)$ is the average displacement for all the elements on the perimeter of the disk. Once the equivalent mass value is extracted from FE simulation, the equivalent stiffness and damping then can be obtained using (25) and (26), and equivalent circuit elements can be determined via (28).

For all devices tested, the agreement between measurement, theory, and finite-element simulation, is quite good. In particular, the agreement between measured, designed, and FE simulated resonance frequencies is less than 1% for disk resonators of all measured sizes, and for all radial-contour modes, from the fundamental on up. Furthermore, the mechanical and electrical equivalent circuit element values extracted from FE simulation match model calculations to within 4%, so the analytical model should be plenty accurate for the design of micromechanical circuits, such as micromechanical filters and oscillators [7], [8], [16], [45].

G. Excessive Series Resistance

As seen in Table I, although the self-aligned disk resonators of this work have now achieved frequencies suitable for RF applications, their series resistances are still excessive, with the smallest measured value of 16.4 kΩ still much larger than exhibited by macroscopic counterparts. As mentioned in Section VII, this large series resistance can be problematic not only in the difficulties it poses for matching to lower impedance off-chip components (e.g., an antenna), but also in its vulnerability to parasitic feedthrough when the resonator is used as an off-chip passive device (i.e., when not directly integrated on-chip with transistors). As explained in Section III, to attain smaller resistances, higher DC-biases and smaller electrode-to-resonator gaps can be used. For example, the use of a 30.54 V DC-bias voltage yields a measured R_x at 737.4 MHz of 62.73 kΩ, which compares well with the 64.45 kΩ predicted by (28), further attesting to its accuracy. In the wake of additional verifications in Table I to back its accuracy, (28) further predicts that R_x's on the order of 300 Ω can be achieved with a DC-bias of 40 V, a resonator disk thickness of 10 μm, an electrode-to-resonator gap spacing of 30 nm, and a reasonably assumed device Q of about 7,900. The complete design for this resonator is summarized in the "Theoretical" column at the far right of Table I, in which deviations from actual fabricated designs to attain small R_x are indicated in bold type. Although 40 V might seem excessive, it is not entirely unreasonable when one considers that it emanates from a charge placed on the resonator, at which no current is flowing, hence no power is consumed. Still, smaller DC-bias voltages are preferred, so research on resonator arrays and alternative resonator designs to lower the required DC-bias voltage is ongoing. Recently, substantial reduction in vibrating micromechanical resonator series motional resistance R_x has been attained via a parallel array of mechanically coupled resonators in which the outputs of several identical micromechanical resonators are summed to obtain a higher output current, and thus a lower effective series resistance, and mechanical coupling is used to ensure matching of the resonances of all resonators in the array. By this means, the motional resistance can be reduced by the number of resonators in the array without sacrificing linearity [50]. Research to apply this technique and others to disk resonators is ongoing.

VIII. Conclusions

By eliminating anchor-to-disk misalignment error through self-alignment, the radial-contour mode polysilicon micromechanical disk resonators of this work have

now achieved frequencies in excess of 1 GHz with Q's still greater than 2,650. In addition, given that the 734.6-MHz disk achieved a frequency Q product of 5.80×10^{12}, which is similar to that of a previous lower frequency (VHF) polysilicon resonator [20], there is evidence that the Q of 2,683 measured for the 1.156-GHz device undershoots the actual value. In particular, even with the conservative assumption that Q might roll off linearly with frequency, this $f_o - Q$ product suggests that the Q's of 5,100 at 1 GHz are not unreasonable. Furthermore, these high-stiffness, high-frequency devices attain almost the same high Q values whether operated in vacuum or air. The implications here are enormous, as this result effectively states that vacuum is no longer needed to attain exceptional Q in high-frequency vibrating micromechanical resonators; rather, only hermetic encapsulation is needed—a fact that should substantially lower the cost of devices based on vibrating RF MEMS technology, making them strong contenders in numerous wireless communication applications, provided impedance matching issues can be alleviated. Research to address impedance matching issues at both the device and system levels is ongoing.

Appendix A
Parameter Extraction from Mixing Measurement Data

The basic theory behind the microelectromechanical mixing concept used in the mixing measurement setup of Fig. 10 already has been covered in [43]. However, because this mixing measurement technique constitutes a less direct measurement of a resonator's frequency response than the more conventional two-port measurement setup of Fig. 2, additional conversion work is required to extract needed parameters from mixing measurement data. In particular, a procedure is required to extract values for the equivalent circuit elements of Fig. 5 from the data in Figs. 12 and 13. This appendix now develops the sequence of expressions needed to perform such an extraction.

To begin, the peak (i.e., resonance) rms power output $P_{o[Measured]}$ from the resonator detected by the spectrum analyzer measurement instrument can be expressed as:

$$P_{o[Measured]} = \frac{1}{2} i_o^2 \times R_L, \text{ where } R_L = 50\Omega, \tag{A1}$$

from which the output current from the resonator can be obtained using:

$$i_{o[Measured]} = \sqrt{\frac{2P_{o[Measured]}}{R_L}}, \text{ where } R_L = 50\Omega. \tag{A2}$$

As described in [43], the mixing drive force generated by the combination of a RF input v_{RF} and a carrier v_{LO} can be written as:

$$F_i = \frac{1}{2} v_{RF} v_{LO} \left(\frac{\partial C}{\partial x}\right)_i = V_P v_{i[Equivalent]} \left(\frac{\partial C}{\partial x}\right)_i, \tag{A3}$$

from which the equivalent input voltage $v_{i[Equivalent]}$ needed to generate the same force by directly exciting the resonator at resonance can be obtained as:

$$v_{i[Equivalent]} = \frac{v_{RF} v_{LO}}{2V_P}. \tag{A4}$$

The measured series motional resistance then can be obtained via the equation:

$$R_{x[Measured]} = \frac{v_{i[Equivalent]}}{i_{o[Measured]}} = \frac{v_{RF} v_{LO}}{2V_P} \times \sqrt{\frac{R_L}{2P_{o[Measured]}}}. \tag{A5}$$

Once $R_{x[Measured]}$ is obtained, values for L_x and C_x can be obtained using:

$$L_x = \frac{QR_{x[Measured]}}{\omega_o}, \tag{A6}$$

$$C_x = \frac{1}{\omega_o^2 L_x}. \tag{A7}$$

As an example, the rms power measured at the peak of the spectrum in Fig. 12(a) is −68.81 dBm, which is 131.5 pW into 50 Ω. Using (A2)–(A4), this corresponds to an rms resonator output current $i_{o[Measured]}$ of 2.294 μA, an equivalent input force F_i of 1.515 μN, and an equivalent input voltage applied to the drive electrode $v_{i[Equivalent]}$ of 1.196 V. Using (A5)–(A7), the above then yield $R_x =$ 519.7 k Ω, $L_x = 0.889$ H, and $C_x = 5.28 \times 10^{-20}$F. These values, as well as those for the other measured spectra, are presented in Table I.

Acknowledgments

The authors would like to thank Dr. John Vig for his many enlightening inputs on phenomena that affect the ultimate stability of micromechanical resonators in general.

References

[1] R. Gregorian and G. C. Temes, *Analog MOS Integrated Circuits for Signal Processing*. New York: Wiley, 1986.

[2] R. A. Sykes, W. L. Smith, and W. J. Spencer, "Monolithic crystal filters," in *IEEE Int. Conv. Rec. Pt. II*, Mar. 20–23, 1967, pp. 78–93.

[3] R. C. Rennick, "An equivalent circuit approach to the design and analysis of monolithic crystal filters," *IEEE Trans. Sonics Ultrason.*, vol. SU-20, pp. 347–354, Oct. 1973.

[4] K. M. Lakin, J. Belsick, J. F. McDonald, and K. T. McCarron, "High performance stacked crystal filters for GPS and wide bandwidth applications," in *Proc. IEEE Ultrason. Symp.*, vol. 1, Oct. 7–10, 2001, pp. 833–838.

[5] C. K. Campbell, *Surface Acoustic Wave Devices for Mobile Wireless Communications*. New York: Academic, 1998.

[6] T. H. Lee and A. Hajimiri, "Oscillator phase noise: A tutorial," *IEEE J. Solid-State Circuits*, vol. 35, pp. 326–336, Mar. 2000.

[7] C. T.-C. Nguyen, "Transceiver front-end architectures using vibrating micromechanical signal processors," in *RF Technologies for Low Power Wireless Communications*. G. I. Haddad, T.

Itoh, and J. Harvey, Eds. New York: Wiley IEEE-Press, 2001, pp. 411–461.

[8] ——, "Transceiver front-end architectures using vibrating micromechanical signal processors," in *Dig. of Papers, Topical Mtg. on Silicon Monolithic Integrated Circuits in RF Systems*. Sep. 12–14, 2001, pp. 23–32.

[9] X. M. H. Huang, C. A. Zorman, M. Mehregany, and M. L. Roukes, "Nanodevice motion at microwave frequencies," *Nature*, vol. 421, p. 496, Jan. 30, 2003.

[10] J. R. Vig and Y. Kim, "Noise in microelectromechanical system resonators," *IEEE Trans. Ultrason., Ferroelect., Freq. Contr.*, vol. 46, pp. 1558–1565, Nov. 1999.

[11] J. R. Clark, W.-T. Hsu, and C. T.-C. Nguyen, "High-Q VHF micromechanical contour-mode disk resonators," *Tech. Dig., IEEE Int. Electron Devices Meeting*, Dec. 11–13, 2000, pp. 493–496.

[12] K. Wang, A.-C. Wong, and C. T.-C. Nguyen, "VHF free-free beam high-Q micromechanical resonators," *IEEE J. Microelectromech. Syst.*, vol. 9, pp. 347–360, Sep. 2000.

[13] W.-T. Hsu and C. T.-C. Nguyen, "Stiffness-compensated temperature-insensitive micromechanical resonators," in *Tech. Digest, 2002 IEEE Int. Micro Electro Mechanical Systems Conf.*, Las Vegas, Nevada, Jan. 20–24, 2002, pp. 731–734.

[14] Y.-W. Lin, S. Lee, S.-S. Li, Y. Xie, Z. Ren, and C. T.-C. Nguyen, "60 MHz wine-glass micromechanical-disk reference oscillator," in *Tech. Dig., ISSCC 2004, San Francisco, CA*, Feb. 6–10, 2004, pp. 322–323.

[15] J. Wang, Z. Ren, and C. T.-C. Nguyen, "Self-aligned 1.14-GHz vibrating radial-mode disk resonators," in *Tech. Dig., 12th IEEE Int. Conf. on Solid-State Sensors Actuators (Transducers '03), Boston, Massachusetts*, Jun. 8–12, 2003, pp. 947–950.

[16] F. D. Bannon, III, J. R. Clark, and C. T.-C. Nguyen, "High-Q HF micromechanical filters," *IEEE J. Solid-State Circuits*, vol. 35, pp. 512–526, Apr. 2000.

[17] C. T.-C. Nguyen, "Micromechanical Signal Processors," Ph.D. dissertation, Department of Electrical Engineering and Computer Sciences, University of California at Berkeley, Dec. 1994.

[18] M. Onoe, "Contour vibrations of isotropic circular plates," *J. Acoust. Soc. Amer.*, vol. 28, pp. 1158–1162, Nov. 1956.

[19] J. R. Clark, W.-T. Hsu, and C. T.-C. Nguyen, "Measurement techniques for capacitively-transduced VHF-to-UHF micromechanical resonators," in *Tech. Dig., 11th IEEE Int. Conf. on Solid-State Sensors Actuators (Transducers '01), Munich, Germany*, June 10–14, 2001, pp. 1118–1121.

[20] M. A. Abdelmoneum, M. U. Demirci, and C. T.-C. Nguyen, "Stemless wine-glass-mode disk micromechanical resonators," in *Proc. 16th Int. IEEE Micro Electro Mechanical Systems Conf.*, Jan. 19–23, 2003, pp. 698–701.

[21] R. A. Johnson, *Mechanical Filters in Electronics*. New York: Wiley, 1983.

[22] C. T.-C. Nguyen, "Frequency-selective MEMS for miniaturized low-power communication devices (invited)," *IEEE Trans. Microwave Theory Tech.*, vol. 47, pp. 1486–1503, Aug. 1999.

[23] W.-T. Hsu, J. R. Clark, and C. T.-C. Nguyen, "A resonant temperature sensor based on electrical spring softening," in *Tech. Dig., 11th Int. Conf. on Solid-State Sensors Actuators (Transducers '01), Munich, Germany*, June 10–14, 2001, pp. 1484–1487.

[24] M. E. Frerking, *Crystal Oscillator Design and Temperature Compensation*. New York: Van Nostrand Reinhold, 1978.

[25] T. Remtema and L. Lin, "Active frequency tuning for micro resonators by localized thermal stressing effects," *Sens. Actuators*, vol. A91, pp. 326–332, 2001.

[26] H. C. Nathanson, W. E. Newell, R. A. Wickstrom, and J. R. Davis, "The resonant gate transistor," *IEEE Trans. Electron. Devices*, vol. ED-14, pp. 117–133, 1967.

[27] W. E. Newell, "Miniaturization of tuning forks," *Science*, vol. 161, pp. 1320–1326, Sep. 1968.

[28] W. C. Tang, T.-C. H. Nguyen, and R. T. Howe, "Laterally driven polysilicon resonant microstructures," *Sens. Actuators*, vol. 20, pp. 25–32, 1989.

[29] L.-Y. Yap, L.-K. Yap, and W. Ye, "Air damping in an ultra-high-frequency disk resonator," in *Tech. Proc. Nanotech. Conf.*, vol. 2, 2003, pp. 444–447.

[30] H. Guckel, D. W. Burns, H. A. C. Tilmans, D. W. DeRoo, and C. R. Rutigliano, "The mechanical properties of fine-grained polysilicon: The repeatability issue," in *Technical Digest, IEEE Solid-State Sensor and Actuator Workshop, Hilton Head Island, SC*, June 1988, pp. 96–99.

[31] G. T. Mulhern, D. S. Soane, and R. T. Howe, "Supercritical carbon dioxide drying of microstructures," in *Tech. Dig., 7th Int. Conf. Solid-State Sens. Actuators (Transducers '93), Yokohama, Japan*, June 1993, pp. 296–299.

[32] J. M. Bustillo, R. T. Howe, and R. S. Muller, "Surface micromachining for microelectromechanical systems," *Proc. IEEE*, vol. 86, pp. 1552–1574, Aug. 1998.

[33] T. A. Core, W. K. Tsang, and S. J. Sherman, "Fabrication technology for an integrated surface-micromachined sensor," *Solid State Technol.*, vol. 36, pp. 39–47, Oct. 1993.

[34] T.-J. King, R. T. Howe, S. Sedky, L. Gang, B. C.-Y. Lin, M. Wasilik, and C. Duenn, "Recent progress in modularly integrated MEMS technologies," in *Tech. Dig., IEEE Int. Electron Device Mtg., San Francisco, CA*, Dec. 8–11, 2002, pp. 199–202.

[35] C. T.-C. Nguyen and R. T. Howe, "An integrated CMOS micromechanical resonator high-Q oscillator," *IEEE J. Solid-State Circuits*, vol. 34, pp. 440–455, Apr. 1999.

[36] A. E. Franke, J. M. Heck, T.-J. King, and R. T. Howe, "Polycrystalline silicon-germanium films for integrated microsystems," *J. Microelectromechan. Syst.*, vol. 12, pp. 160–171, Apr. 2003.

[37] X. Xiao, J. Birrell, J. E. Gerbi, O. Auciello, and J. A. Carlisle, "Low temperature growth of ultrananocrystalline diamond," *J. Appl. Phys.*, vol. 96, pp. 2232–2239, Aug. 2004.

[38] J. H. Smith, S. Montague, J. J. Sniegowski, J. R. Murray, and P. J. McWhorter, "Embedded micromechanical devices for the monolithic integration of MEMS with CMOS," in *Tech. Dig., IEEE Int. Electron Device Mtg., Washington D.C.*, Dec. 10–13, 1995, pp. 609–612.

[39] A. Singh, D. A. Horsley, M. B. Cohn, A. P. Pisano, and R. T. Howe, "Batch transfer of microstructures using flip-chip solder bonding," *IEEE J. Microelectromech. Syst.*, vol. 8, pp. 27–33, Mar. 1999.

[40] A.-C. Wong, Y. Xie, and C. T.-C. Nguyen, "A bonded-microplatform technology for modular merging of RF MEMS and transistor circuits," in *Tech. Dig., 11th Int. Conf. on Solid-State Sensors Actuators (Transducers '01), Munich, Germany*, June 10–14, 2001, pp. 992–995.

[41] A. N. Karanicolas, "A 2.7-V 900-MHz CMOS LNA and mixer," *IEEE J. Solid-State Circuits*, vol. 31, pp. 1939–1944, Dec. 1996.

[42] C. T.-C. Nguyen, "Electromechanical characterization of microresonators for circuit applications," M.S. Report, Department of Electrical Engineering and Computer Sciences, University of California at Berkeley, Apr. 1991.

[43] A.-C. Wong and C. T.-C. Nguyen, "Micromechanical mixer-filters ("mixlers")," *IEEE/ASME J. Microelectromech. Syst.*, vol. 13, pp. 100–112, Feb. 2004.

[44] J. Wang, Z. Ren, and C. T.-C. Nguyen, "1.14-GHz Self-aligned vibrating micromechanical disk resonator," in *Proc. IEEE MTT-RFIC Symp.*, June 8–10, 2003, pp. 335–338.

[45] K. Wang and C. T.-C. Nguyen, "High-order medium frequency micromechanical electronic filters," *IEEE/ASME J. Microelectromech. Syst.*, vol. 8, pp. 534–557, Dec. 1999.

[46] W. T. Hsu, S. Lee, and C. T.-C. Nguyen, "In situ localized annealing for contamination resistance and enhanced stability in nickel micromechanical resonators," in *Digest of Technical Papers, 10th Int. Conf. Solid-State Sensors Actuators, Sendai, Japan*, June 7–10, 1999, pp. 932–935.

[47] C. D. Stockbridge, "Effects of gas pressure on quartz crystal microbalances," in *Vacuum Microbalance Techniques*. vol. 5, New York: Plenum, 1966, pp. 147–178.

[48] C. T.-C. Nguyen and R. T. Howe, "Microresonator frequency control and stabilization using an integrated micro oven," in *Digest of Technical Papers, 7th Int. Conf. Solid-State Sensors Actuators (Transducers '93), Yokohama, Japan*, June 7–10, 1993, pp. 1040–1043.

[49] T. V. Rozhart, "The effect of thermoelastic internal friction on the Q of micromachined silicon resonators," in *Technical Digest of the IEEE Solid-State Sensor Actuator Workshop, Hilton Head, SC*, June 4–7, 1990, pp. 13–16.

[50] M. U. Demirci, M. A. Abdelmoneum, and C. T.-C. Nguyen, "Mechanically corner-coupled square microresonator array for reduced series motional resistance," in *Dig. of Tech. Papers, 12th Int. Conf. on Solid-State Sensors Actuators (Transducers '03), Boston, MA*, June 8–12, 2003, pp. 955–958.

Jing Wang (S'02) received dual B.S. degrees in Mechanical Engineering and Electrical Engineering from Tsinghua University, Beijing, China, in 1994, and dual M.S. degrees in Electrical Engineering and Computer Science and Mechanical Engineering from the University of Michigan at Ann Arbor, in 2000 and 2002, respectively. He is currently working toward the Ph.D. degree at the University of Michigan.

From 1993 to 1994, he was an intern at OMRON, where he participated in the development and configuration of DeviceNet, a network technology designed to meet the performance and reliability requirements of the industrial environment. His research interests include microfabrication technologies, new materials for RF MEMS applications, merged circuit microelectromechanical technologies, and integrated circuit design and technology.

Mr. Wang was the recipient of the Third Best Student Paper Award at the IEEE 2003 Radio Frequency Integrated Circuits Conference (RFIC).

Zeying Ren received the B.S. and M.S. degrees in Electrical Engineering from Tianjin University, P.R. China, in 1987 and 1990, respectively.

From 1990 to 1998, she was a Process Engineer in the National Research Center for Optoelectronics (NCOT) in the Institute of Semiconductors at the Chinese Academy of Science. She had been employed as Research Scholar in the Department of Electrical and Computer Engineering at Northwestern University from 1998 through 2000.

In 2001, she joined Nanovation Technologies as a Process Engineer. In 2002, she joined the Solid State Electronics Laboratory (SSEL) as an Engineer in Research, in the Department of Electrical Engineering and Computer Science at University of Michigan, Ann Arbor, where she presently focuses on MEMS fabrication.

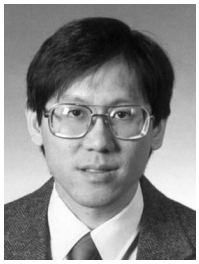

Clark T.-C. Nguyen (S'90–M'95–SM'01) received the B.S., M.S., and Ph.D. degrees from the University of California at Berkeley in 1989, 1991, and 1994, respectively, all in Electrical Engineering and Computer Sciences.

In 1995, he joined the faculty of the University of Michigan, Ann Arbor, where he is presently an Associate Professor in the Department of Electrical Engineering and Computer Science. His research interests focus upon micro electromechanical systems (MEMS) and include integrated micromechanical signal processors and sensors, merged circuit/micromechanical technologies, RF communication architectures, and integrated circuit design and technology. From 1995 to 1997, he was a member of the National Aeronautics and Space Administration (NASA)'s New Millennium Integrated Product Development Team on Communications, which roadmapped future communications technologies for NASA use into the turn of the century. In 2001, Prof. Nguyen founded Discera, Inc., a company aimed at commercializing communication products based upon MEMS technology, with an initial focus on the very vibrating micromechanical resonators pioneered by his research in past years. He served as Vice President and Chief Technology Officer (CTO) of Discera until mid-2002, at which point he joined the Defense Advanced Research Projects Agency (DARPA) on an IPA, where he is presently the Program Manager of the MEMS, Micro Power Generation (MPG), Chip-Scale Atomic Clock (CSAC), MEMS Exchange (MX), Harsh Environment Robust Micromechanical Technology (HERMIT), Micro Gas Analyzers (MGA), Radio Isotope Micropower Sources (RIMS), and RF MEMS Improvement (RFMIP) programs, in the Microsystems Technology Office of DARPA.

Prof. Nguyen received the 1938E Award for Research and Teaching Excellence from the University of Michigan in 1998, an EECS Departmental Achievement Award in 1999, the Ruth and Joel Spira Award for Teaching Excellence in 2000, and the University of Michigan's 2001 Henry Russel Award. Together with his students, he received the Roger A. Haken Best Student Paper Award at the 1998 and the 2003 IEEE International Electron Devices Meetings.